Global and local heat transfer behaviour of a three-dimensional Pulsating Heat Pipe: combined effect of the heat load, orientation and condenser temperature

Global and Local Heat Transfer Behaviour of a three-dimensional Pulsating Heat Pipe: Combined Effect of the Heat Load, Orientation and Condenser Temperature

Luca Pagliarini[a], Luca Cattani[b], Mauro Mameli[d], Sauro Filippeschi[d], Fabio Bozzoli[a,c,*], Sara Rainieri[a,c]

[a] Department of Engineering and Architecture, University of Parma, Parco Area delle Scienze 181/A, Parma, Italy
[b] CIDEA Interdepartmental Centre, University of Parma, Parco Area delle Scienze 181/A, Parma, Italy
[c] SITEIA.PARMA Interdepartmental Centre, University of Parma, Parco Area delle Scienze 181/A, Parma, Italy
[d] Department of Energy, Systems Land and Construction Engineering, University of Pisa, Largo L. Lazzarino, Pisa, Italy

[*]E-mail: fabio.bozzoli@unipr.it

Abstract. Pulsating Heat Pipes having non-planar layouts (i.e. three-dimensional layouts) are preferable to the planar geometries when both gravity-independency and compactness are needed. A multi-turn three-dimensional Closed Loop Pulsating Heat Pipe is tested on ground with the aim of investigating the effects of gravity by means of a quantitative description of the working modes occurring during its operation at different orientations. The viscous effects are furthermore considered by varying the condenser temperature. The studied device is made of an annealed aluminium tube (Inner/Outer diameter: 3/5 mm), folded in 14 turns and partially filled with methanol (volumetric filling ratio: 0.5). The channels are externally coated with a black high-emissivity paint, thus allowing the measurement of the outer wall temperature in the whole adiabatic section by means of a high-speed Medium Wave InfraRed camera. The wall temperature and the fluid pressure are instead monitored by means of thermocouples and pressure transducers directly inserted in the fluid stream. The Pulsating Heat Pipe global performance is first assessed by evaluating the equivalent thermal resistance for every test case, showing that the studied three-dimensional layout is independent of gravity at high power input levels, where the equivalent thermal resistance settles around 0.25 K/W for almost every orientation. The thermographic acquisitions are therefore post-processed to estimate the heat flux locally exchanged between the working fluid and the channels wall, and the resulting local wall-to-fluid heat fluxes are statistically reduced for the quantification of the observed working modes, i.e. pure conduction, start-up, intermittent flow and full activation. At high heat loads to the evaporator, the gravity-independent behaviour of the device is found to be promoted by full activations, i.e. when a regular fluid motion is perceivable in every branch within the adiabatic section. The flow modes are also identified, pointing out that the local heat transfer behaviour is capable of discerning fluid oscillations from net fluid circulations. All the qualitative and quantitative pieces of data are comprehensively presented to give further information regarding the device dependency on the orientation. To deeper investigate the link between local and global quantities, the equivalent thermal resistance is finally compared with the statistical coefficients provided by the local heat transfer analysis.

Keywords: Pulsating Heat Pipe, Three-dimensional layout, Orientation, Inverse Heat Transfer, Thermal Performance, Working Modes.

1. Introduction

The electrical energy demand for the cooling of electronic systems by active two-phase heat transfer devices is more and more increasing due to the continuous miniaturization process of electronic components, resulting in higher power densities to be dissipated [1]. Two-phase passive devices, such as Heat Pipes (HPs) and Pulsating Heat Pipes (PHPs), represent a suitable solution for this challenging thermal management issue. PHPs are achieving resounding interest within the scientific community due to their

low manufacturing cost, good surface adaptability and high flexibility [2], when compared to the "wicked" devices. Although the PHP working principles are still not fully understood, many parameters, such as the internal diameter, the working fluid, the filling ratio, the number of turns and the orientation, have been found to influence the device performance in terms of heat transfer capabilities [3]. Specifically, the effects of gravity on the device operation have been intensively studied on planar and tubular geometries, showing that the PHP thermal performance is strongly dependent on the device orientation, i.e. the position of the evaporator and the condenser with respect to the gravity field. In fact, PHPs usually exhibit lower activation power inputs when the inclination is increased with respect to the horizontal orientation and the device benefits from the assistance of gravity [4]. On the other hand, the evaporator dry-out (i.e. the cold fluid in the condenser is not able go back to the evaporator, resulting in a rapid increase in the evaporator temperature [9]), is influenced by the orientation since the critical power input given to the evaporator generally increases with the PHP tilting angle [5]. However, such dependency represents a drawback from an application standpoint, especially when the device performance is required to be independent from the orientation and the power input level. For this reason, researchers explored the possibility to reduce such dependency by studying alternative geometries. Specifically, the operation of planar PHPs was found to be acceptably independent of the inclination angle for high number of turns ([6], [7], [8]), i.e. high number of heated zones. The increase in the number of turns anyhow results in larger device dimensions, thus narrowing the range of applicability to those applications that do not impose limiting geometrical constraints. Hence, 3D layouts (i.e. non-planar layouts) are preferable to the planar ones when both gravity-independency and compactness are needed. In addition, 3D PHPs might present enhanced thermal performances with respect to the planar layouts even in the most unfavourable orientations, i.e. low inclination angles [7], making these geometries worth of investigation. Yang et al. [9] studied the operational limits of 3D Closed Loop PHPs (CLPHP) made of 40 copper tubes. For inner/outer diameter equal to 1 mm and 2 mm, respectively, the CLPHP equivalent thermal resistance assumed similar values for every considered inclination angle and power input to the evaporator, thus suggesting the independency of the device performance from the orientation. By increasing the inner/outer diameter to 2 mm and 3 mm, respectively, both the horizontal orientation and the Top Heated Mode (THM) (i.e. vertical with the condenser zone below the evaporator zone) exhibited instead a strong drop in performance with respect to the Bottom Heated Mode (BHM), i.e. vertical with the evaporator zone below the condenser zone. Yet, no data related to the PHP start-up were provided. Qu et al. [10] analysed a 3D PHP having 12 heated zones and inner/outer diameter equal to 2/3 mm. For the horizontal orientation, the activation heat load was found to be slightly lower than that assessed for the BHM, in disagreement with the thermal behaviour typical of planar geometries, while, at high power inputs, the BHM exhibited the best thermal performance. However, by increasing the number of heated zones to 16 [11], the device performance was comparable for every orientation, thus underlining the beneficial effect of a higher number of turns, even though the best performance at low power inputs was still found for the BHM. An interesting comparison between the three-dimensional and the bi-dimensional layout was also presented, verifying that the 3D geometry enhances the heat transfer capabilities in the horizontal orientation with respect to the 2D layout, especially at high heat loads. Tseng et al. [12] tested a 3D CLPHP with 12 heated zones, focusing on the counter-gravity effects, i.e. by comparing the BHM with the THM. The results pointed out that, although the device activation was strongly hampered in counter-gravity, the device performance at high heat loads was comparable between the two operation modes.

Although some parameters, e.g. the number of turns and the inner/outer diameter, have been found to guarantee the independency of three-dimensional layouts from the orientation within certain heat load ranges, the gravity effects are not still fully clarified, in particular for the antigravity operation (THM). This may be due to the fact that the PHP performance and, more precisely, the working modes occurring during the device operation are generally investigated by means of global quantities, such as wall temperature fluctuations at the condenser/evaporator section, thus undermining the full comprehension of the device thermal response.

The present experimental study proposes to describe the working modes at varying orientations by means of a local quantity, i.e. the heat flux exchanged between the working fluid and the device channels wall, thus attempting to explain the relation between the independency from gravity and the thermo-fluid dynamics of the working fluid in 3D layouts. The local wall-to-fluid heat flux is estimated within the whole adiabatic section of a 3D CLPHP, already tested in weightless conditions [13], to give information about the entire device by means of the inverse approach presented in [14].

The CLPHP is first characterized by evaluating its equivalent thermal resistance at every considered orientation, namely the horizontal orientation, the vertical BHM and the vertical THM. The viscous effects are furthermore investigated by considering different condenser temperatures. Statistical parameters, based on the variations of the local wall-to-fluid heat flux from channel to channel during the pseudo steady-state of the device, are therefore evaluated to quantify the PHP working modes for each power input given to the evaporator. They are also identified to give a better insight into the device heat transfer modes. A comparison between the evaluated statistical quantities and the equivalent thermal resistance is finally presented to provide a comprehensive description of the device operation in terms of both local and global behaviour.

2. *Experimental facilities and image processing procedure*

The studied device (Fig. 1) is made of an annealed aluminium tube (6060 alloy, I/O diameter = 3/5 mm), shaped in a 3D closed loop layout (overall size: 220x80x25 mm, 14 turns). Such peculiar 3D geometry is specifically designed to fit the limiting constrains of the Heat Transfer Host aboard the International Space Station [13]. Two aluminium heat spreaders (100x12x10 mm) are brazed on the tube in the evaporator zone, holding two ceramic ohmic heaters (Innovacera®, electrical resistance 18 Ω ± 10). The evaporator section is insulated by means of a layer (0.01 m) of insulating material. The heating power is provided by a programmable power supply (GW-Instek®, PSH-6006A). The condenser zone is embedded between two aluminium heat spreaders (80x120x10 mm, Fig. 1b), cooled by means of a Peltier cell system (eight Peltier cells by Adaptive Thermal Management®, ETH-127-14-11-S; control system by Meertstetter Engineering®, TEC 1123) coupled with a cold plate temperature control system loop (Aavid Thermalloy®). The temperature of the evaporator is measured through five T-type thermocouples located between the evaporator spreader and the heater, while the temperature at the condenser is monitored by six T-type thermocouples located between the Peltier cold side and the condenser aluminium heat spreader and two placed on the condenser heat spreader. All the thermocouples were calibrated with a thermal chamber (BINDER®) and a reference four wire Pt-100 (ITS-90 standard, max. error 0.035 K).

a)

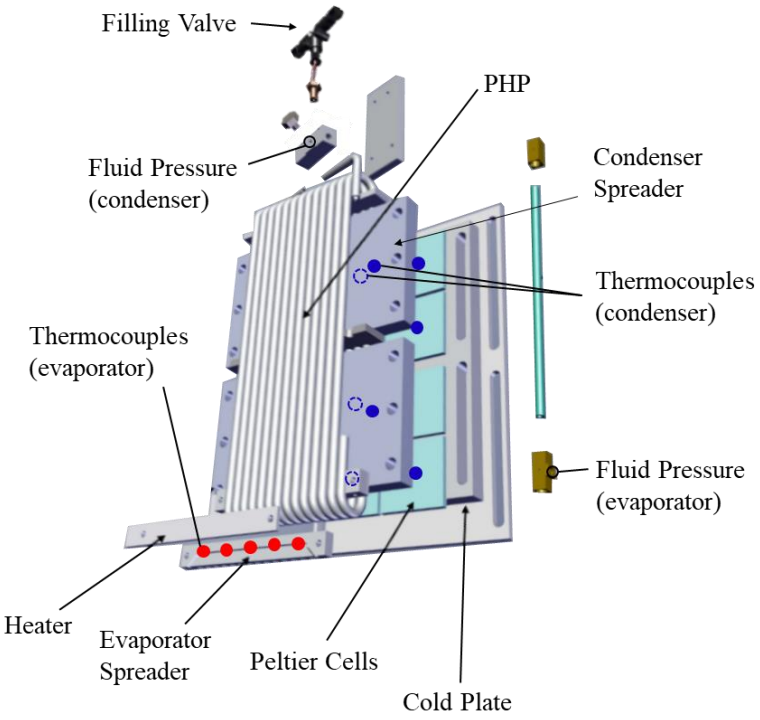

b)

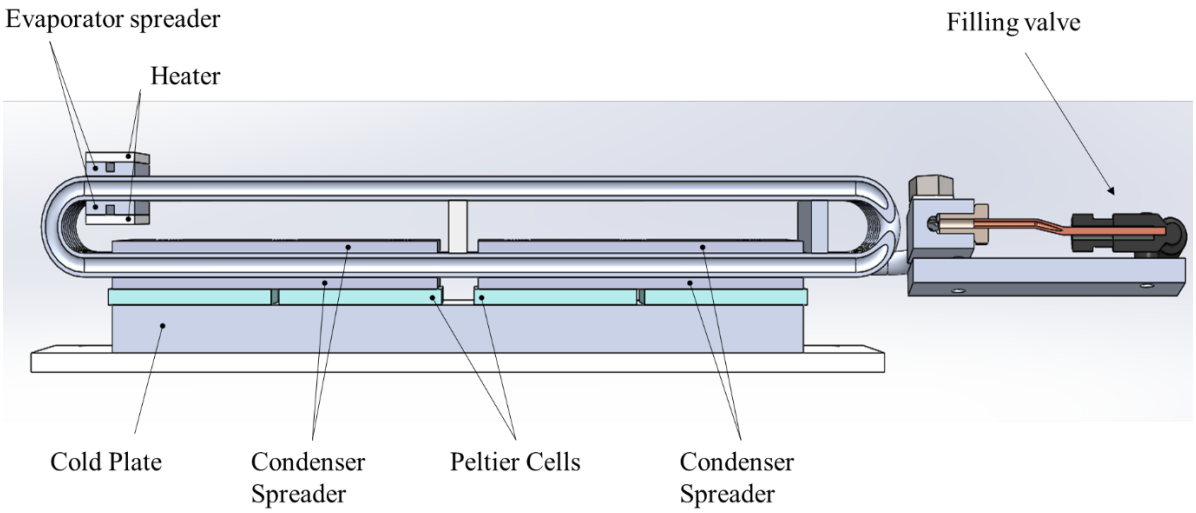

Figure 1: Exploded view and measurement tools location (a); sectional view (b).

The fluid pressure at the condenser and evaporator sections were measured by two miniature pressure transducers (Keller® PAA-M5-HB, 1 bar abs, 0.2% FSO accuracy), directly inserted in the fluid stream. All the thermocouples' signals were recorded at 10 Hz, while the pressure measurements were sampled at 18 Hz.

The aluminium channels within the adiabatic section were uniformly coated with a high-emissivity opaque paint ($\varepsilon = 0.92$), and the temperature was acquired by a high-resolution Medium Wave InfraRed (MWIR) camera (FLIR® SC7600, 18 Hz, 640x512 pixels).

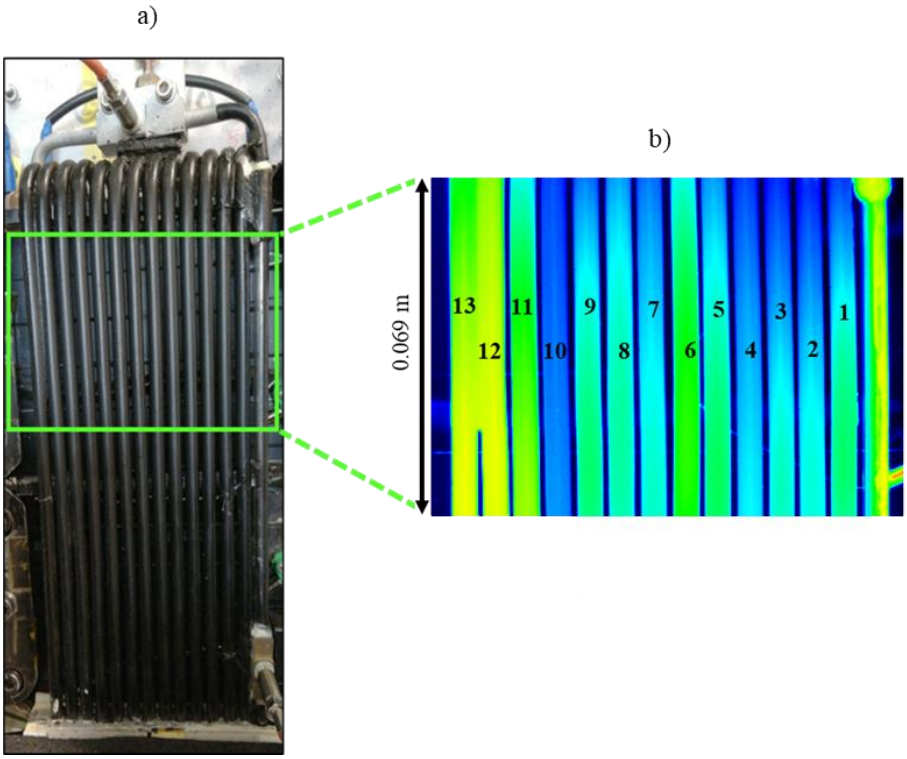

Figure 2: Section framed by the MWIR camera (a) and sample of infrared acquisition (b), used as reference for the aluminium channels' numeration.

The InfraRed (IR) measurements were carried out in between the evaporator and the condenser within a 0.069 meters long section (Fig. 2) since the adiabatic zone was the only portion directly accessible to the IR camera. The 13 aluminium channels are numbered starting from the one next to the sapphire insert.

The uncertainty related to each measured parameter [13], as provided by the manufacturers, is listed in Table 1.

Table 1: uncertanty of the measurement tools.

Parameter	**Specs**	**Sampling frequency**	**Uncertainty**
Channel wall temperature	T-type Thermocouple (0.5 mm bead diameter)	10 Hz	± 0.1°C
	High-speed Medium Wave Infrared Camera	18 Hz	± 0.2°C
Fluid temperature	Omega® KMTSS-IM025E-150 K-Type thermocouple (0.25 mm bead diameter)	10 Hz	± 0.2°C
Fluid pressure	Keller® PAA-M5-HB, 1 bar abs	18 Hz	± 500 Pa
Power Input	GW-Instek®, PSH-6006A	-	± 2 W

The device was first vacuumed (down to 10^{-6} mbar) and then partially filled by means of a micro-metering valve (IDEX® Upchurch Sc. P- 447) with methanol (filling ratio = 50 ± 1% vol.). Specifically, methanol was used among other fluids due to its relatively low dynamic viscosity and high latent heat, but mostly because it guarantees the presence of a capillary flow inside the device, according to the static criterion, i.e. Bond number less than 4 [2], even if the 3 mm internal diameter is rather big with respect to the values that can be commonly found in the literature. The Authors are aware that the chemical compatibility level of aluminium and methanol is not recommended for long-terms applications due to the generation of Non-Condensable Gases (NCGs) [15]. However, the relatively short duration of the tests (~ 2 months) resulted in a negligible production of NCGs. Despite the fact that the obtained outcomes may not be fully exploited for an immediate industrial application, they are certainly interesting from a physical point of view, thus improving the understanding of phenomenological aspects and providing useful references for the validation of numerical models present in the literature.

Before the filling procedure, the working fluid was degassed in a secondary tank by continuous boiling: incondensable gases thus accumulated in the upper part of the tank and they were therefore sucked from above by means of several vacuuming cycles with the same procedure described by Henry et al. [16].

During the experiments, the device was tested in horizontal orientation, vertical Bottom Heat Mode (BHM) and vertical Top Heated Mode (THM), as shown in Fig. 3.

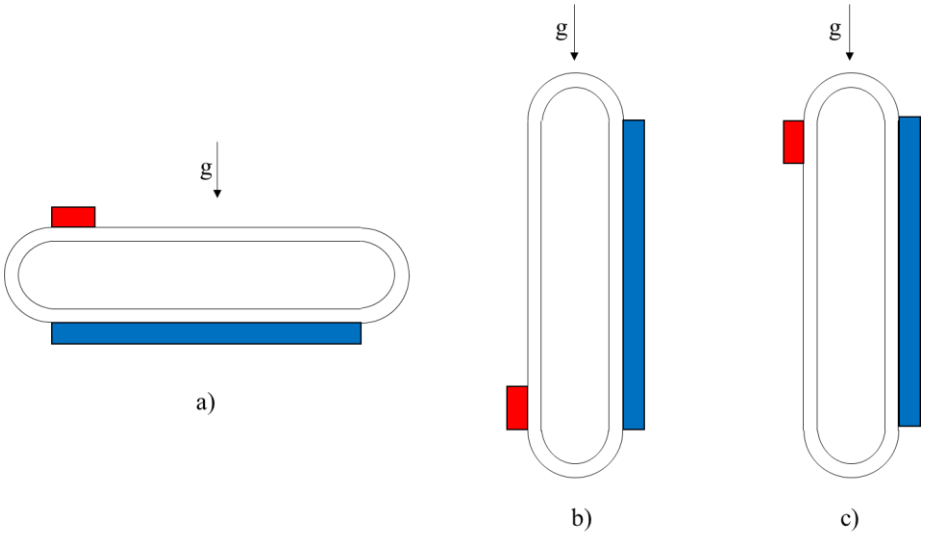

Figure 3: Sketch of the considered PHP orientations, depending on the heat source position (red) with respect to the heat sink (blue) and the gravitational field g: horizontal orientation (a), BHM (b) and THM (c).

The condenser temperature T_{cond} was set to 10°C and 20°C for each orientation mode, while the heat load to the evaporator was varied from 10 W up to a maximum of 210 W. For every combination of condenser temperature and device orientation, two IR acquisitions (60 seconds each) were carried out within the pseudo-steady states of the system, i.e. after about 25 minutes from each heat load step to the evaporator.

For safety reasons, the evaporator temperature was limited to a maximum of 105°C by a thermal switch, directly placed on the evaporator heater.

3. Local heat flux estimation procedure

The local convective heat flux q, exchanged at the inner wall, i.e. the fluid-wall interface, was evaluated starting from the temperature distribution on the channels outer surface acquired by the IR camera within the adiabatic section.

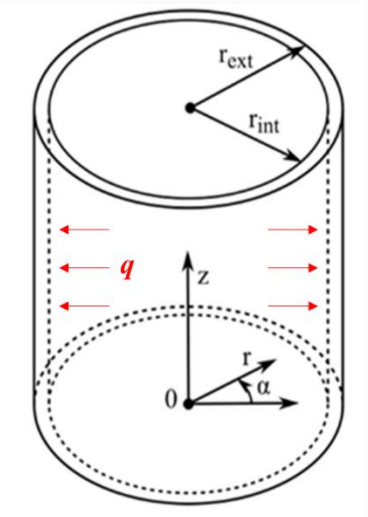

Figure 4: Sketch of the test section.

As already pointed out by Pagliarini et al. [14], the test section, outlined in Fig. 4, can be modelled as an axisymmetric 1D domain by considering negligible the temperature gradient along the circumference. The thin wall approximation is furthermore adopted.

Starting from the local energy balance equation at the infinitesimal wall section, the heat flux on the wall inner surface can be obtained from the following equation, thoroughly explained in [14]:

$$q = \frac{\left(\rho c_p \frac{\partial T}{\partial t} - k \frac{\partial^2 T}{\partial z^2}\right) \cdot \left(r_{ext}^2 - r_{int}^2\right) + \frac{(T - T_{env})}{R_{env}} \cdot 2r_{ext}}{2r_{int}} \tag{3}$$

where k is the thermal conductivity of the aluminium channel (201 W/mK at 300 K), T_{env} is the environmental temperature and R_{env} is the overall heat-transfer resistance between the channel wall and the surrounding environment, assumed equal to 0.1 m^2K/W, which is a representative value for air natural convection with radiative heat transfer towards the environment. A sensitivity analysis carried out on eq. (3) highlighted that reasonable variations of R_{env} provides negligible variations of q, especially at high heat loads, where the storage term $\rho c_p \frac{\partial T}{\partial t}$ has peaks of the order of magnitude of 10^4 W/m^2. Being the measured wall temperature unavoidably noisy, eq. (3) gives unstable results since the derivative operators are very sensitive to small perturbations in the input data when coupled with the negative effect of noise [17]. The n^{th} derivative is a linear operator that behaves as a filtering operator with a gain that amplifies the high−frequency components of a given set of input data more than the low−frequency ones. In almost all practical situations regarding heat transfer, the frequency components of the exact signal concentrate in the low-frequency range of the spectrum, whereas the noise, which is usually Gaussian, is uniformly distributed in the high-frequency domain. Consequently, the Laplacians of the raw data cannot be directly calculated due to the noise level. A convenient way to overcome these difficulties is filtering out the unwanted noise from the raw temperature data [18-20]. The application of a Gaussian filter, defined by the transfer function of eq. (4) along the two dimensions u and v (representative of t and z), reduces the data high-frequency components.

$$H(u, v) = e^{-(u^2+v^2)/2u_c^2} \tag{4}$$

Since in real applications the optimal cut-off frequency u_c value is not known a priori, in the present analysis the criterion provided by the discrepancy principle, originally formulated by Morozov [21], was adopted. According to this principle, the problem solution is regarded to be sufficiently accurate when the difference between the measured T and filtered T_f temperatures is close to the standard deviation of the raw measurements:

$$\frac{\left\|T_f - T\right\|_2}{\sqrt{N \cdot M}} \cong \sigma \tag{5}$$

where $\left\| \ \right\|_2$ stands for the 2-norm, N and M are the sizes of the T matrix (N axial coordinates, M time samples) and σ is the standard deviation of the raw data, estimated by measuring the wall temperature distribution while maintaining the system under isothermal conditions. σ was found to vary from 0.04 K at high temperature, i.e. for PHP configurations at T_{cond} = 20°C, to 0.06 K at low temperature, i.e. for PHP configurations at T_{cond} = 10°C, due to the specific specifications of the adopted MWIR camera.

By adopting the filtered temperature T_f, eq. (3) can be finally solved by means of the finite difference method.

The effectiveness of the Gaussian filter was quantified by using synthetic data, representative of the oscillatory behaviour of the studied device, as inputs for dedicated CFD simulations. The estimation

error was assessed to be directly proportional to the oscillation frequency and inversely proportional to the amplitude of the local wall-to-fluid thermal interactions. Specifically, the estimation error ranged from about 9% of the evaluated q for low frequencies and high amplitudes, to a maximum of 21% for high frequencies and low amplitudes. The method, as well as the error analysis, is shown in detail in a previous work by the same Authors [14].

4. Results

The investigated PHP configurations are summarized in Table 2. Specifically, the thermal switch activation was avoided by setting, case by case, different upper limits to the providable power input to the evaporator Q.

Table 2: Studied PHP configurations and provided power inputs.

Orientation	T_{cond} **[°C]**	**Range of** Q **[W]**
Horizontal	20	10 up to 190
BHM	20	10 up to 190
THM	20	10 up to 180
Horizontal	10	10 up to 190
BHM	10	10 up to 210
THM	10	10 up to 150

4.1 Global performance

For every studied configuration, the PHP thermal characterization was first achieved by evaluating the equivalent thermal resistance R_{eq}, defined by eq. (6) as a function of the net power input provided to the evaporator Q_{net} [3]:

$$R_{eq} = \frac{T_{eva} - T_{cond}}{Q_{net}} \tag{6}$$

Considering the thermal conductivity of the insulation layer (0.02 W/mK), the difference between the evaporator and the environmental temperature ($\Delta T \approx 50$ K for the most unfavourable condition), and the total external surface of the evaporator insulation (0.0034 m^2), the heat losses to the environment in the evaporator section are always less than the 0.5% of the heat load provided by the heater and they are consequently neglected in the present study.

For the present study case, both T_{eva} and T_{cond} were evaluated by averaging the wall temperature at the two PHP sections, measured by means of the thermocouples over the last 5 minutes within the pseudo-steady state. By adopting the approach by Kline and McClintock [22], the uncertainty on R_{eq} was assessed to have a maximum of about 15% at very low heat loads and a minimum around 0.6% at high heat loads. Specifically, calling $\delta_{\Delta T}$ the uncertainty related to the temperature difference $\Delta T = T_{eva} - T_{cond}$ and δ_Q the uncertainty related to the provided heat load Q, the uncertainty on the equivalent thermal resistance is computed as $\delta_{R_{eq}} = \sqrt{\left(\frac{1}{\Delta T}\delta_{\Delta T}\right)^2 + \left(\frac{1}{Q}\delta_Q\right)^2}$.

The thermal resistance referred to the empty device was found to be equal to 1.4 K/W; this value is representative of the heat transferred by only conduction through the aluminium tube between the heated and the cooled section. Such resistance was evaluated for power inputs up to 50 W, since higher heat loads brought to the system overheating and to the consequent activation of the thermal switch.

In Fig. 5a, the equivalent thermal resistance is shown, with the corresponding error bars, for every PHP orientation and condenser temperature as a function of Q.

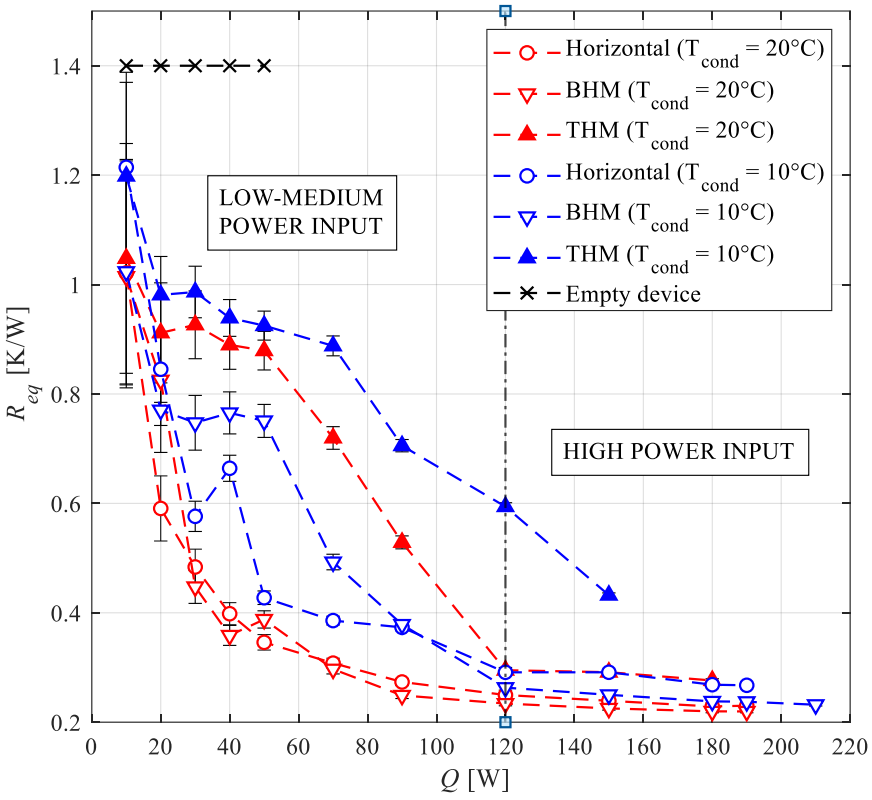

Figure 5: Equivalent thermal resistance of the device as a function of the power input Q, evaluated for every considered orientation and condenser temperature.

Here, two main effects are expected to affect the device thermal performance: the viscous effects, related to a lower functioning temperature of the device, and the gravity effects, related to the PHP orientation with respect to the gravitational field.

Since the fluid viscosity is inversely proportional to the fluid temperature, the fluid motion damping increases when the condenser temperature is set to the lowest value T_{cond} = 10°C (blue trends in Fig. 5a). Consequently, R_{eq} assumes higher values with respect to the configurations at T_{cond} = 20°C (red trends in Fig. 5a). In fact, for low fluid temperatures (from 10°C to 20°C), the variation of fluid viscosity μ with respect to temperature $\frac{\partial \mu}{\partial T} \approx$ -1·10^{-5} Pa·s/K, while, for high fluid temperatures (higher than 30°C), $\frac{\partial \mu}{\delta T} \approx$ -7.3 ·10^{-6} Pa·s/K. This results in a percent variation of viscosity of about -25 % and -6 % at low and high temperatures, respectively, thus denoting stronger viscosity effects at lower values of $T_{cond,}$ i.e. lower fluid temperature.

Regarding the effect of the orientation on the device thermal performance, two different zones are defined according to the heat load given to the evaporator: the low/medium power input zone (Q < 120 W), where these effects are more evident and the trends vary in a wider range of thermal resistances, and the high power input zone ($Q \geq$ 120 W), where R_{eq} is less dependent both on the heat load and the orientation. In the low/medium power input zone, the horizontal orientation (circles in Fig. 5a) is characterized by values of thermal resistance which decrease almost monotonically with the increase of the power input given to the evaporator for both condenser temperatures. The BHM (downward triangles in Fig. 5a) presents instead two different trends from one condenser temperature to the other: at T_{cond} = 20°C, R_{eq} is comparable with the thermal resistance trend observed in the horizontal orientation for the same condenser temperature, while, at T_{cond} = 10°C, R_{eq} settles around 0.76 K/W to start decreasing from 50 W. Hence, the BHM configurations, when compared with the horizontal modes, denote similar performances at low heat loads. Although such evidence disagrees with various literature

findings related to the planar devices [4], the enhanced PHP thermal response at low power inputs in the horizontal orientation was found to be comparable with the one assessed in [10] for a similar 3D geometry. In fact, in 3D layouts, the presence of small gravity heads, even when they are not favourable, may assist the triggering of the fluid motion.

Regarding the THM (upward triangles in Fig. 5a), the device exhibits a low performance at low power inputs due to the counter-gravity effects, which strongly hamper the fluid motion.

In the high power input zone, the considered geometry may be responsible for the high PHP thermal performances, denoted by R_{eq} values which stabilizes around 0.25 K/W for all the configurations but the THM at T_{cond} = 10°C. The device thus seems not to be significantly affected either by the orientation or by the condenser temperature at high heat loads, confirming the results found in previous works ([11,12]). It must be pointed out that such interesting inclination-independent feature is not generally obtained for planar layouts having similar geometry, number of turns and working fluid. Verma et al. [23] studied a 6-turn planar PHP with inner diameter of 1.45 mm, showing that, when the device was filled with methanol, its equivalent thermal resistance was higher for the horizontal orientation with respect to that for the vertical orientation. Similar outcomes were found by Mameli et al. [24] and Ayel et al. [25].

The thermal behaviour in the THM at T_{cond} = 10 °C leads to the highest global thermal resistance values in the investigated power input range. However, the trend of R_{eq} (Q) is sharply decreasing, and it may reach lower values if power inputs would be higher than 150 W. The test was stopped here not because of a dry-out event, but due to safety issues, since the heater temperature overcome 105 °C and the thermal switch cut off the power supply.

4.2 Local analysis

In order to provide a deeper insight into the heat transfer phenomena occurring in the device, a local heat transfer analysis was carried out for every PHP working configuration. To this aim, the IR acquisitions on the adiabatic section were post-processed by means of the procedure presented in Section 3, resulting in N×M time-space heat flux distributions referred to each of the 13 analyzed channels. Since the heat losses to the environment within the whole adiabatic section, for the most unfavourable test condition, i.e. Q = 210 W, were lower than 3 W (average wall temperature ≈ 50°C), the IR measurements were assumed to perceive temperature variations due to the inner thermal interactions between the channel wall and the working fluid rather than between the channel wall and the environment. Such assumption can be extended to every study case since the heat losses to the environment span from about 0.7 % of the total provided power input at low heat loads to about 1.5 % at high heat loads.

The wall temperature distribution (Fig. 6a) and the corresponding wall-to-fluid heat flux distribution (Fig. 6d) are reported for channel 4 (horizontal orientation, T_{cond} = 20°C, Q = 120 W), together with their space distribution for 4 different time instants (Fig. 6b and 6d, respectively).

a)

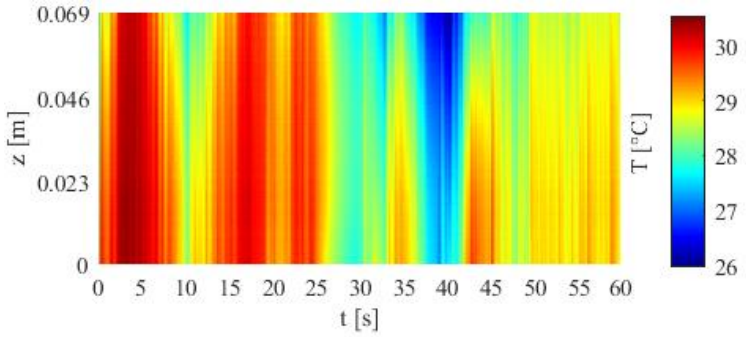

b)

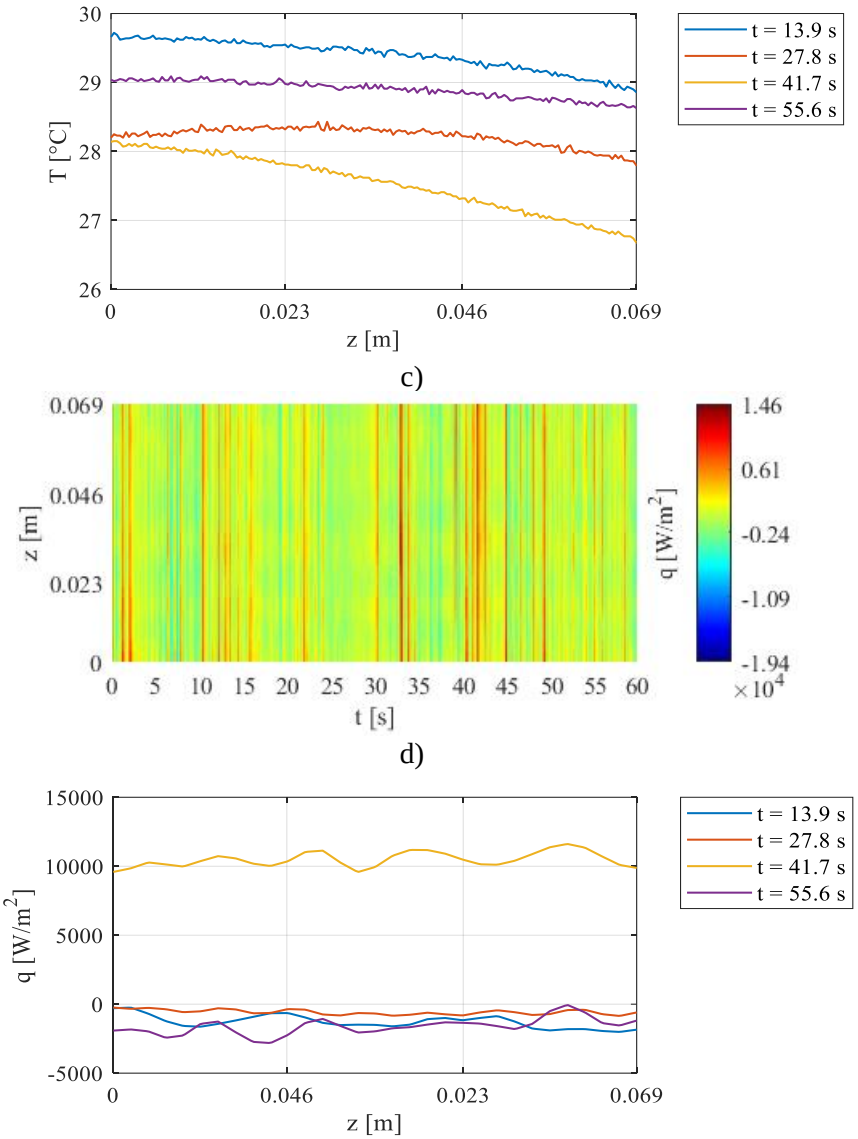

Figure 6: Raw IR measurement (a) and its space distribution for 4 different time instants (b); evaluated wall-to-fluid heat flux (c) and its space distribution for 4 time instants (d). Channel 4, horizontal orientation, Q = 120 W, T_{cond} = 20°C.

According to the adopted reference system, the heat flux distribution assumes positive values when the heat flux is transferred from the fluid to the channel wall. As already stated in [14] and [26], some information regarding the fluid motion inside the channel can be obtained without a direct fluid visualization. In fact, the thermographic measurements on the tube outer surface performed on the same device were found to successfully catch transient phenomena that occur inside the PHP tube in a time higher than 0.3 s [14], e.g. hot or cold fluid oscillations between the evaporator and condenser section. Hence, positive heat fluxes may correspond to the passage of hot vapor plugs and liquid slugs from the evaporator to the condenser. On the other hand, negative heat fluxes may generally denote flow reversal phenomena, during which cold fluid flows from the condenser to the evaporator at a lower temperature than that of the channel wall, previously heated by hot fluid coming from the evaporator. However, every other significantly faster transient phenomenon, e.g. alternance of liquid slugs and vapour plugs in the fluid flow, could not be fully perceived on the outer surface due to the filtering effect of the aluminium wall, as noticeable from Figs. 6b-d.

4.3 Systematic detection of the PHP working modes

The study of the PHP working modes, coupled with the device global performance evaluation, is crucial for the achievement of a comprehensive description of the device heat transfer capability at varying working conditions. In fact, the different working modes define the heat transfer modes obtained by means of the thermally induced fluid motion between the evaporator and the condenser section [27].

In the available literature, the PHP working modes are generally characterized from a qualitative point of view by means of either an optical visualization of the fluid motion/flow pattern, performed when the PHP presents transparent inserts, or the detection of temperature oscillations over the entire device, performed instead when a direct visualization cannot be achieved. From the latter approach, four main working modes can be identified during the pseudo-steady state before the occurrence of the dry-out [2] as follows:

- pure conduction (or device inactivity), where the wall temperature at both the evaporator and the condenser section presents no fluctuations (the heat is only transferred by conduction);
- start-up (or device activation), where wall temperature variations start to be perceivable within the evaporator section at least in one channel;
- intermittent flow, where the evaporator temperature does not stabilize due to the occurrence of multiple stop-overs;
- full activation, where the evaporator temperature either abruptly decreases or exhibits weak fluctuations [28].

In the present work, a novel objective mode detection method is adopted, based on the post-processing of the IR measurements on the adiabatic section through analytical (IHCP solution approach) and statistical tools recently proposed in transient conditions by Pagliarini et al. [14]. Specifically, such method can be performed on opaque tubes in a repeatable and comparable way for any tubular PHP geometry or experimental condition by using the heat flux locally exchanged within the adiabatic section between the working fluid and the PHP walls.

It must be pointed out that the local investigation on the PHP heat transfer behaviour within the adiabatic zone has been proven to perceive fluid motion in the overall device alike direct fluid visualizations, thus providing complementary definitions of the working modes with respect to those presented by means of the only evaporator/condenser temperature measurements [14]:

- when the device is not yet activated, the local wall-to-fluid heat flux is almost null in every PHP channel;
- the device start-up occurs when at least one channel locally presents slight heat flux variations over time;
- during the intermittent flow mode, the heat flux oscillates in multiple PHP branches. From a local point of view, the device stop-overs are to be intended as periodic deactivations of some PHP channels, where the wall-to-fluid heat flux alternates oscillations to almost null values;
- full activation, where every PHP branch presents regular oscillations over time of the wall-to-fluid heat flux.

In the present investigation, the working modes occurring during the device operation were identified by adopting both the evaporator temperature and the wall-to-fluid heat flux fluctuations within the adiabatic section to give an insight into the heat transfer behaviour of the studied PHP. First, the history of the evaporator temperature over the entire duration of the tests was adopted as reference for the identification of the device working modes at different heat loads for every studied configuration, [2]. Fig. 7 shows the evaporator temperature trends for two configurations, namely the horizontal orientation, T_{cond} = 10°C (Fig. 7a) and the BHM, T_{cond} = 20°C (Fig. 7b). In Fig. 7a, the evaporator temperature starts to present appreciable fluctuations from 20 W, which persist also during the pseudo-steady state of the device, thus denoting the device activation. By increasing the heat load up to 120 W, the evaporator temperature presents, in every measurement point, an alternance of high and low peaks, suggesting the occurrence of several stop-overs typical of the intermittent flow mode [2]. From 150 W

up to the maximum provided power input, the temperature fluctuations are more stable in time, thus denoting the full activation of the device [28]. By carrying out a similar analysis on the data provided in Fig. 7b, the activation of the device was observed at 30 W, the intermittent flow mode was assessed in the range 40 to 70 W, while the full activation of the device occurred from 90 W up to 190 W.

a)

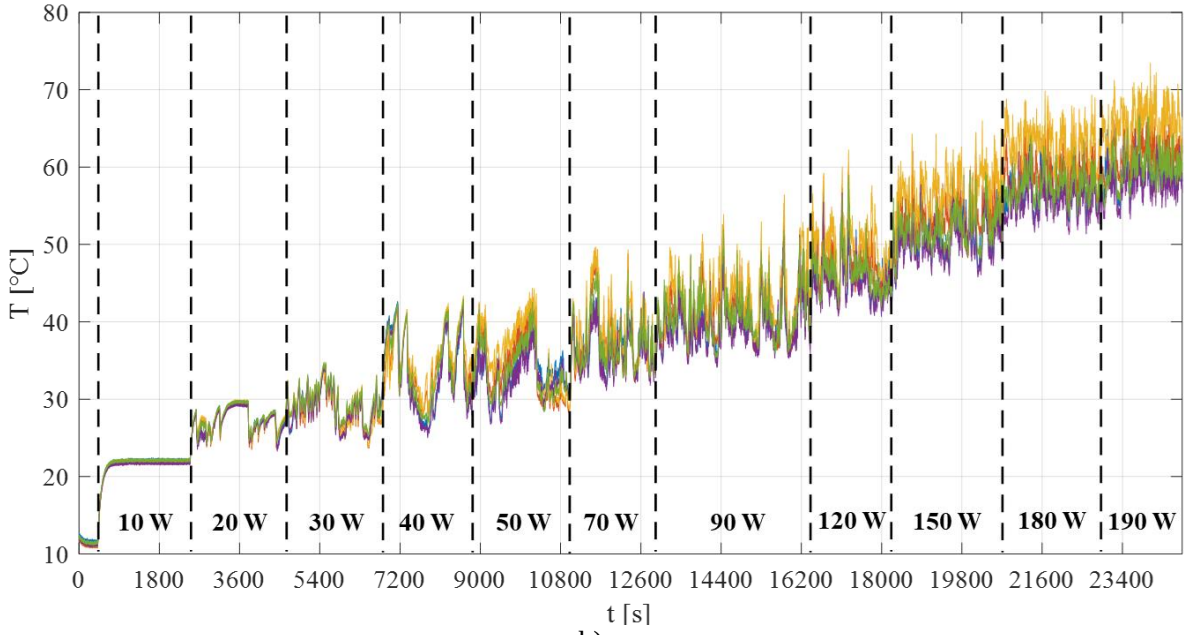

b)

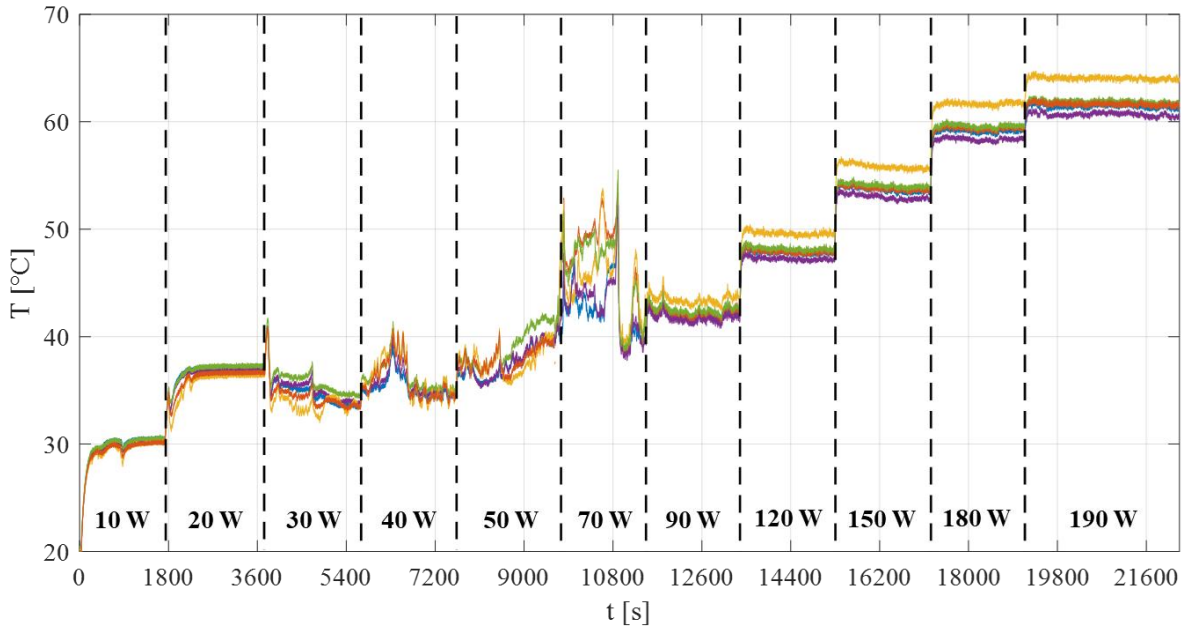

Figure 7: History of the evaporator temperature over the entire duration of the tests for the horizontal mode, T_{cond} = 10°C (a) and the BHM, T_{cond} = 20°C (b).

The evaporator temperature variations were therefore compared with the evaluated local wall-to-fluid heat flux within the adiabatic section to provide an additional reference for the identification of the PHP working modes. For every tested configuration, the evaporator temperature, measured at five different locations over 6 minutes within the pseudo-steady state of the system, was compared with the local wall-to-fluid heat flux exchanged through channel 1, 4, 7 and 10 (reference of Fig. 2) for the axial

coordinate z = 0.035 over 1 minute, together with its error bars (black lines, according to the estimation error provided in Section 3).

In Fig. 8, three different study cases were chosen as representative samples for the mentioned working mode identification procedure. In the THM, for Q = 10 W and T_{cond} = 20°C (Fig. 8a-b), the device exhibits a pure conduction working mode since the evaporator temperature is greatly stable (Fig. 8a) and the local heat flux is almost null (Fig. 8b), thus denoting the absence of fluid motion. In the BHM, for Q = 90 W and T_{cond} = 10°C (Fig. 8c-d), the evaporator temperature presents instead strong variations due to device stop-overs (Fig. 8c). Similarly, the wall-to-fluid thermal interactions within the adiabatic section are characterized, in every considered channel, by null local heat fluxes, followed by slight heat flux peaks (Fig. 8d), suggesting that the device is operating in an intemittent way. Specifically, by comparing Fig. 8c and Fig. 8d, while the evaporator temperature is almost stable from t = 300 s to 340 s, it undergoes an overall increase from t = 340 s to 360 s, typical of a fluid motion stop-over phenomenon. Such behaviour is strictly linked to the local wall-to-fluid heat flux. In fact, during the first seconds of the observation window, q presents weak fluctuations in every channel, while, during the last seconds of acquisition, q is almost null in every PHP branch, highlighting that evaporator and the condenser sections are not thermally interacting, i.e. the heat provided to the evaporator is not being effectively dissipated. Finally, in the horizontal orientation, for Q = 180 W and T_{cond} = 10°C, the PHP is fully activated. In fact, the evaporator temperature (Fig. 8e) presents relatively low deviations with respect to its mean value, while the heat fluxes (Fig. 8f) denote strong and persistent fluid oscillations between the evaporator and the condenser section in the overall device.

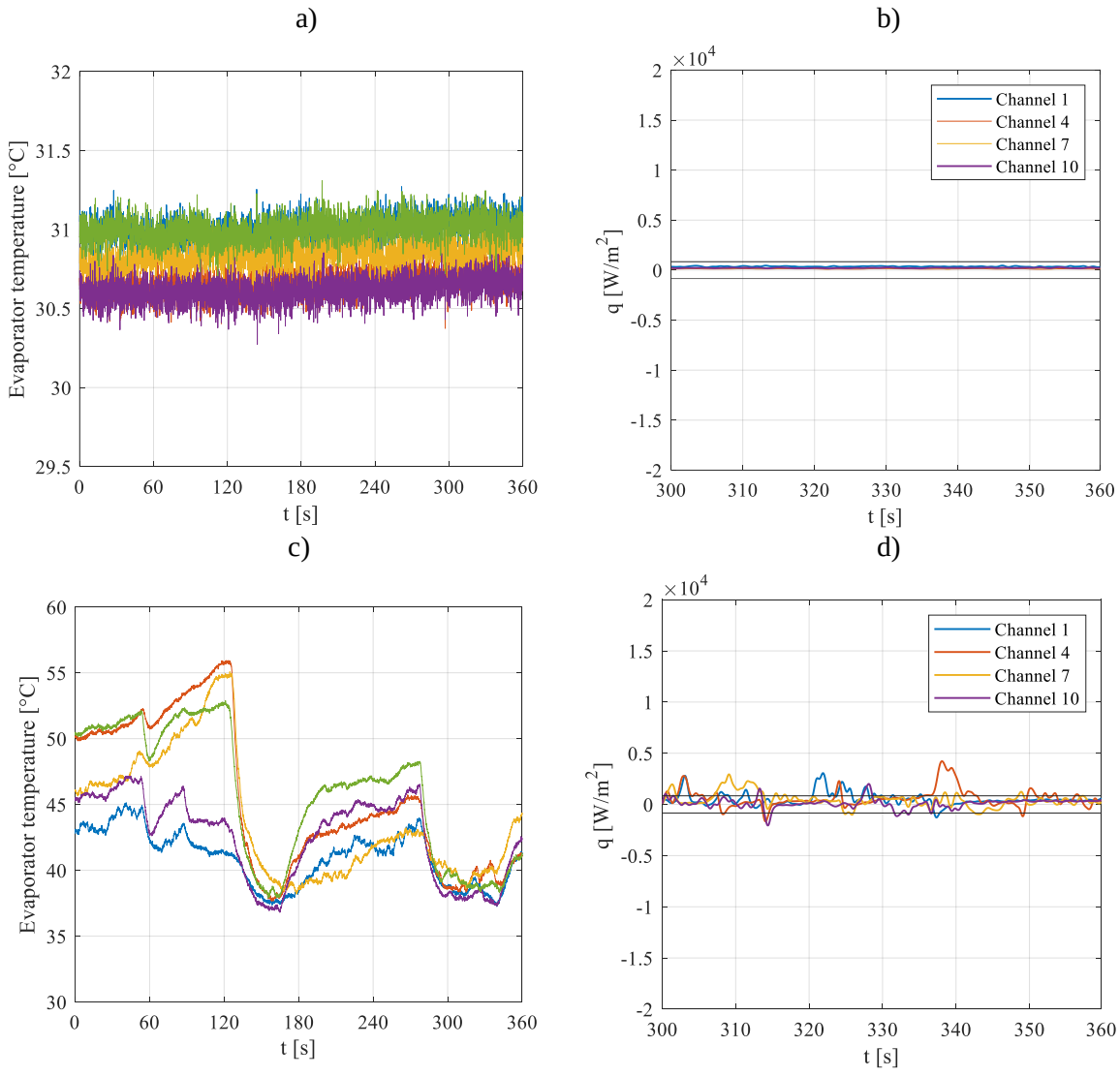

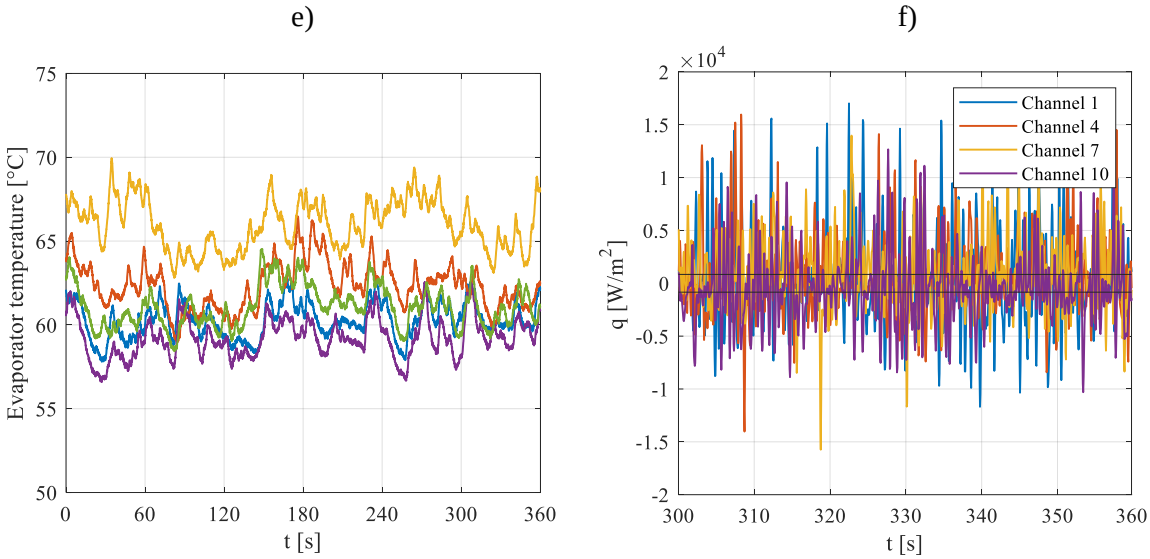

Figure 8: Evaporator temperature and local heat flux evaluated on 4 PHP channels together with its error bars (black lines), for the THM, Q = 10 W, T_{cond} = 20°C (a,b), the BHM, Q = 90 W, T_{cond} = 10°C (c,d) and the horizontal orientation, Q = 180 W, T_{cond} = 10°C (e,f).

The PHP working modes, observed by replicating the above evaluation for every studied configuration, are summarized in Table 3. Here, the horizontal orientation is characterized by low activation power inputs to the evaporator, and the intermittent flow mode persists for a wider range of power inputs with respect to the BHM. In fact, for such orientation, the gravity tends to promote a stable fluid oscillation in the whole PHP, thus anticipating at lower heat loads the full activation of the device. Within the THM, the device operates instead in a narrow range of heat loads, and it generally does not work in a satisfactorily way, especially at low condenser temperature. Moreover, both the BHM and the THM seem to be strongly influenced by the condenser temperature at low heat loads due to a strong delay of activation from T_{cond} = 20°C to T_{cond} = 10°C.

Table 3: Device working modes for different PHP configurations and power inputs to the evaporator Q. "-": device inactivity (pure conduction), "S": start-up, "I": intermittent flow, "FA": device full activation.

	***Q* [W]**											
	10	*20*	*30*	*40*	*50*	*70*	*90*	*120*	*150*	*180*	*190*	*210*
Orientation	***T_{cond} = 20°C***											
Horizontal	-	*S*	*I*	*I*	*I*	*I*	*I*	*FA*	*FA*	*FA*	*FA*	
BHM	-	-	*S*	*I*	*I*	*I*	*FA*	*FA*	*FA*	*FA*	*FA*	
THM	-	-	-	-	*S*	*I*	*I*	*FA*	*FA*	*FA*		
	T_{cond} = 10°C											
Horizontal	-	*S*	*I*	*I*	*I*	*I*	*I*	*I*	*FA*	*FA*	*FA*	
BHM	-	-	-	-	-	*S*	*I*	*FA*	*FA*	*FA*	*FA*	*FA*
THM	-	-	-	-	-	-	*S*	*I*	*I*			

The regime limits in terms of heat input level may slightly vary between the cases where the heat loads are increasing (heat load ramp-up) or decreasing (heat load ramp-down) due to hysteresis

phenomena, as also shown by Mameli et al. [5]. Nevertheless, from the start-up point of view, the "heat ramp-up" procedure used here is the most conservative between the two because the fluid activation energy must be provided to trigger the flow motion. Finally, for what concerns the repeatability, the Authors tested the same configurations several times, confirming that each operating regime occurs accordingly to those shown in table 3. To provide a quantitative and repeatable identification of the working modes at different heat loads in pseudo-steady state conditions, the statistical coefficient of variation over time *cvt*, defined by eq. (7) for the n-th channel, is introduced:

$$cvt_n = \frac{\sum_{i=1}^{N}\left[\frac{std(|q_n(i,t=1,\dots,M)|)}{mean(|q_n(i,t=1,\dots,M)|)}\right]}{N} \tag{7}$$

where q_n is the N×M (axial coordinates × time instants) heat flux distribution referred to the n-th PHP channel, *std* stands for the standard deviation and *mean* stands for the arithmetic mean. Such coefficient is chosen among other statistical quantities since it has already been proven to satisfactorily identify wall-to-fluid heat flux variations over time [14]. Although the wall-to-fluid heat fluxes are defined as time-space distributions, the heat flux along the axial coordinate was not similarly investigated since the present device does not allow to perceive significant heat flux space variations, mainly due to the filtering effects of the aluminium walls [14].

The statistical coefficient cvt_n describes the irregularity of the fluid oscillations in terms of heat flux amplitude in each PHP channel over time: for high cvt_n values, the fluid oscillations are strongly irregular, denoting an alternation of time intervals in which the heat flux is oscillating from positive to negative values and time intervals in which it is almost null. Low values of cvt_n denote instead regular oscillations of the heat flux with almost regular amplitudes over time. As reference for the regularity of the oscillations, sinusoidal functions (maximum oscillation regularity) present coefficient of variation almost equal to 50%, while constant functions present coefficient of variation equal to 0%. cvt_n was evaluated by means of eq. (7) for each PHP configuration. In particular, the number of statistically reduced samples was equal to the number of time instants M, (M = 1080, corresponding to 60 seconds), for both the *std* and the *mean* operators, while the average over N considered the number of axial coordinates (N = 195, corresponding to 0.069 m), thus ensuring the robustness of the adopted statistical approach.

Furthermore, the cvt_n values referred to each channel were expressed in terms of average value (cvt_{av}) and standard deviation (cvt_{std}) on the overall device by considering the 13 analysed aluminium channels as follows:

$$cvt_{av} = \frac{\sum_{n=1}^{13} cvt_n}{13} \tag{8}$$

$$cvt_{std} = \sqrt{\frac{\sum_{n=1}^{13}(cvt_n - cvt_{av})^2}{13}} \tag{9}$$

From a physical point of view, since cvt_n quantifies the variation over time of the heat flux for the n-th channel, cvt_{av}, defined by equation 8, describes how the heat flux varies, on average, over the whole device. Furthermore, cvt_{std}, defined by equation 9, describes the dispersion of cvt_n around its average in the whole PHP, thus quantifying the variations in local thermal behaviour from channel to channel.

cvt_{av} and cvt_{std} are shown in Fig. 9a and 9b, respectively, as a function of *Q*.

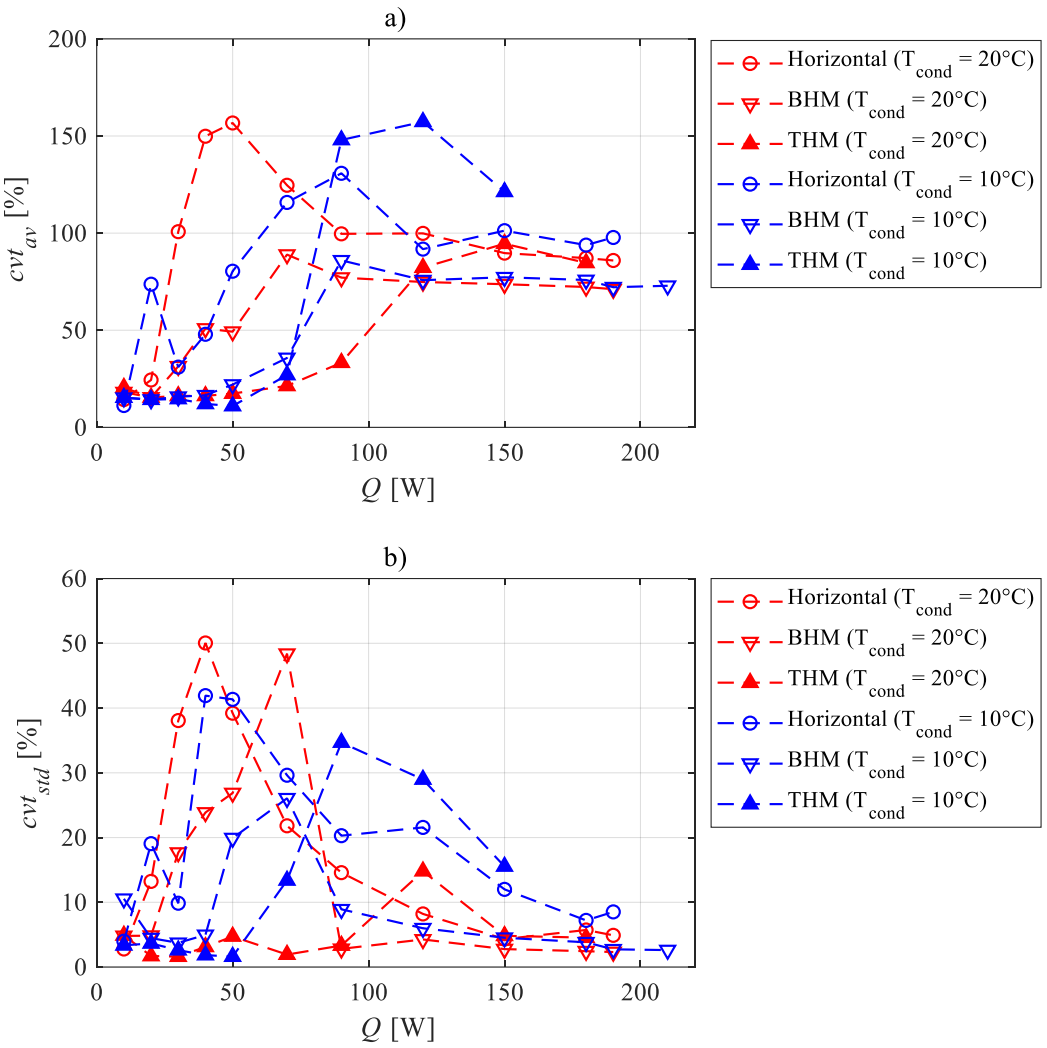

Figure 9: cvt_{av} (a) and cvt_{std} (b) against the power input to the evaporator for every PHP configuration.

Hence, the PHP working modes, qualitatively identified in Table 3, can be quantified as follows:

- PHP inactivity, described by values of cvt_{av} and cvt_{std} in the range 10 to 20% and 0 to 10%, respectively, due to almost null exchanged heat fluxes within the observation windows;
- PHP start-up, where both cvt_{av} and cvt_{std} exceed the inactivity threshold of 20% and 10%, respectively;
- intermittent flow, described by values of cvt_{av} and cvt_{std} which increase up to about 155% and 50%, respectively, due to significantly different heat transfer phenomena involving each channel;
- full activation, where cvt_{av} stabilizes in the range 70 to 100% and cvt_{std} settles in the range 0 to 15%, denoting that the fluid motion is perceivable in every PHP branch and the fluid oscillations are regular. Specifically, cvt_{av} is in the range 86 to 100% for both the horizontal orientation and the THM, while the BHM is characterized by lower values of such statistical quantity (70 to 78%).

4.4 Fluid flow modes detection: oscillatory VS circulatory

The PHP heat transfer behaviour is not only defined by the different working modes occurring during the device operation, but also by the different fluid flow modes, namely the fluid oscillation and the fluid net circulation. Specifically, the net fluid circulation, when compared to the oscillatory flow, usually guarantees a lower and more stable evaporator temperature at high power inputs [29], thus improving the device thermal performances.

To achieve a better understanding of the heat transfer modes of the device, different PHP configurations were considered with the aim of assessing the presence of either fluid oscillation or circulation. In graphs of Fig. 10(a-c-e), the thermocouples signals referred to the evaporator section are plotted for three different test cases, i.e. horizontal mode (Q = 120 W), BHM (Q = 120 W) and THM (Q = 150 W) for the same condenser temperature T_{cond} = 20°C, over one minute within the pseudo-steady state. For the same cases, ΔP, defined as the difference between the fluid pressure measured near the evaporator and the condenser in a single PHP channel (Fig. 1a), is reported in Fig. 10(b-d-f), as well as its moving average over time (red line). The window length for the moving average was chosen equal to 2 seconds to remove the high-frequency noisy components from the analysis without having a loss of information regarding the stable oscillations of pressure signals. ΔP represents the driving force for the fluid motion, and it has been already proven to be a useful quantity for the fluid motion assessment within the PHP branch where the pressure transducers are placed [13]. In fact, when ΔP assumes positive values, the fluid flows through the channel from the evaporator to the condenser, while, for negative ΔP values, flow reversals phenomena occur in the same branch. By comparing graphs of Fig. 10(a-c-e), the evaporator temperature is clearly more stable within the BHM (Fig. 10c). Moreover, while the ΔP referred to both the horizontal orientation (Fig. 10b) and the THM (Fig. 10f) oscillates from positive to negative values, i.e. its moving average varies around zero, the ΔP related to the BHM (Fig. 10d) is positive over almost the whole observation window, i.e. its moving average assumes only positive values, thus denoting that the fluid circulates from the evaporator to the condenser without any flow reversals. The presented analysis was replicated for every test case, highlighting that the circulatory flow occurs only within the BHM mode, in accordance with previous works [2]. In particular, the heat loads required for the device to operate in a circulatory mode were found to be in the ranges 90 to 190 W and 120 to 210 W for T_{cond} = 20°C and T_{cond} = 10°C, respectively.

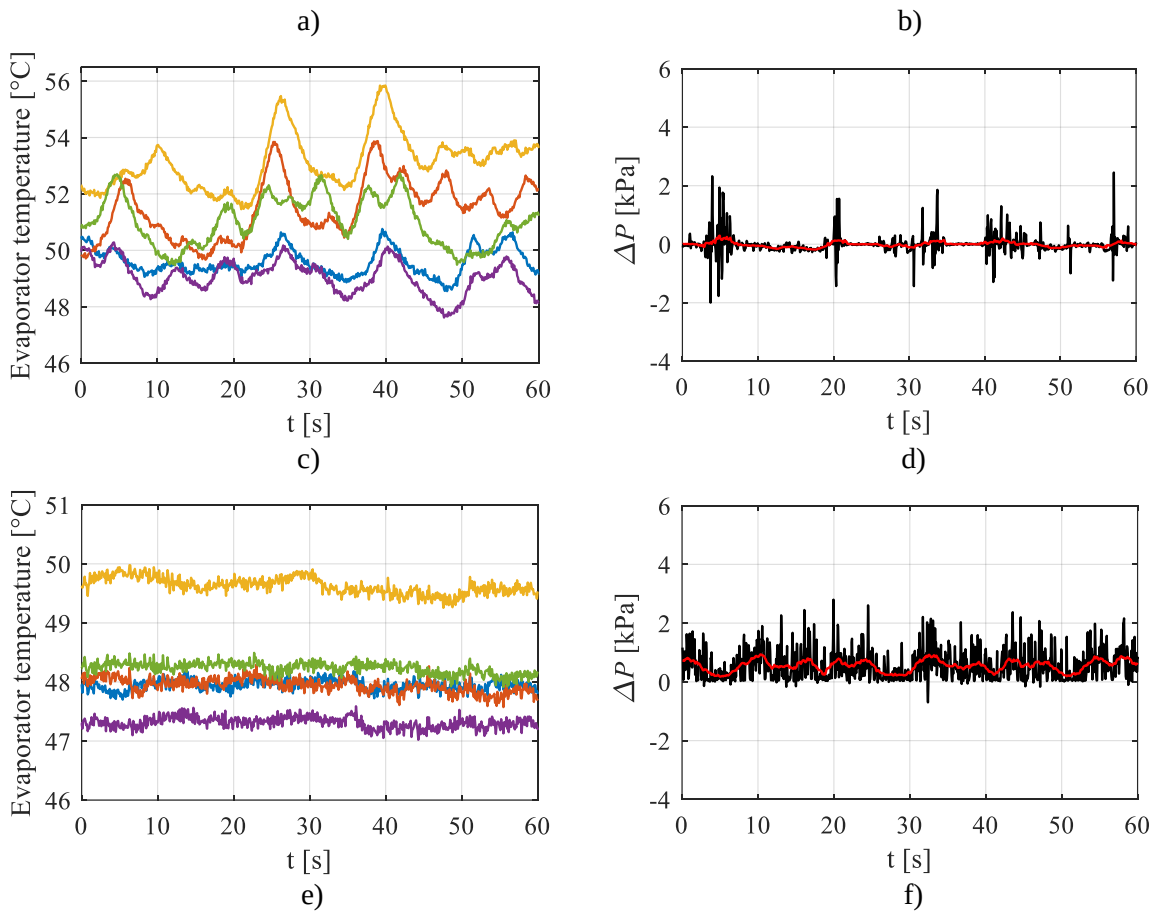

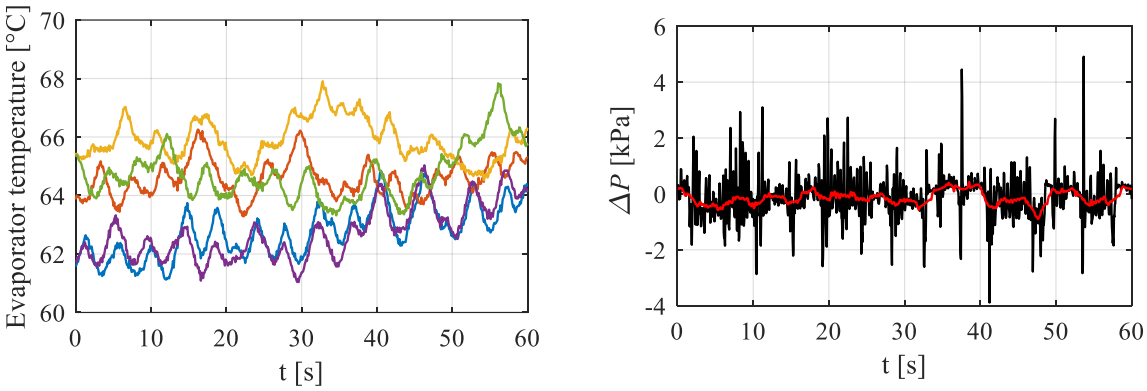

Figure 10: Thermocouples signals referred to the evaporator section and corresponding ΔP (red line: moving average over time). Horizontal orientation, Q = 120 W (a,b); BHM, Q = 120 W (c,d); THM, Q = 150 W (e,f), T_{cond} = 20°C.

To provide a further validation of the oscillatory/circulatory flow detection procedure presented above, the local heat transfer properties were therefore investigated. To this aim, the local heat flux distributions over time, referred to each PHP branch, were adopted for the evaluation of normalized cross correlations between adjacent channels.

In particular, the normalized cross correlation between two finite discrete functions of time *f(t)* and *g(t)* is defined as [30]:

$$r = (f \star g)[\tau] = \sum_{t=0}^{T-1} \overline{f[t]}\, g[(t+\tau)_{modT}] \tag{10}$$

where τ is the displacement (or lag) between f and g and T is the total number of time samples. $\overline{f(t)}$ denotes the complex conjugate of *f(t)*, while the subscript *modT* denotes the modulo operator. Eq. (10) essentially shifts the function *g(t)* along the time axis, calculating, for each single shift τ, the sum of the product between *f(t)* and *g(t)*. Hence, when a proper overlap of the two functions is reached, r is maximized and the time lag between the original signals can be assessed. Other lower-amplitude peaks of r depend on the shape of the given functions and they are not to be considered as representative of the actual time delay. To provide an example for the interpretation of the r function, two arbitrary signals are introduced as follows and plotted in Fig. 11a:

$$f(t) = \sum_{i=1}^{4} \frac{1}{i} \cdot \sin\left[2\pi t(0.4 + 0.2i)\right] \tag{11}$$

$$g(t) = 1.5 \cdot f(t) \tag{12}$$

Their normalized cross correlation is shown in Fig. 11b: since the two signals are perfectly in phase, the lag between the two functions equals zero and r assumes a maximum peak (r = 1) at τ = 0 s. By considering a different case, in which $f(t)$ is shifted of 0.3 seconds with respect to $g(t)$ (Fig. 11c), the normalized cross correlation (Fig. 11d) assumes a peak (r = 0.98) at τ = 0.3 s, thus verifying the capability of the function r to assess the time lag between two given signals, whether they are in phase or not. It must be pointed out that τ can assume both positive and negative values: when $\tau > 0$, g is in advance with respect to f.

a) b)

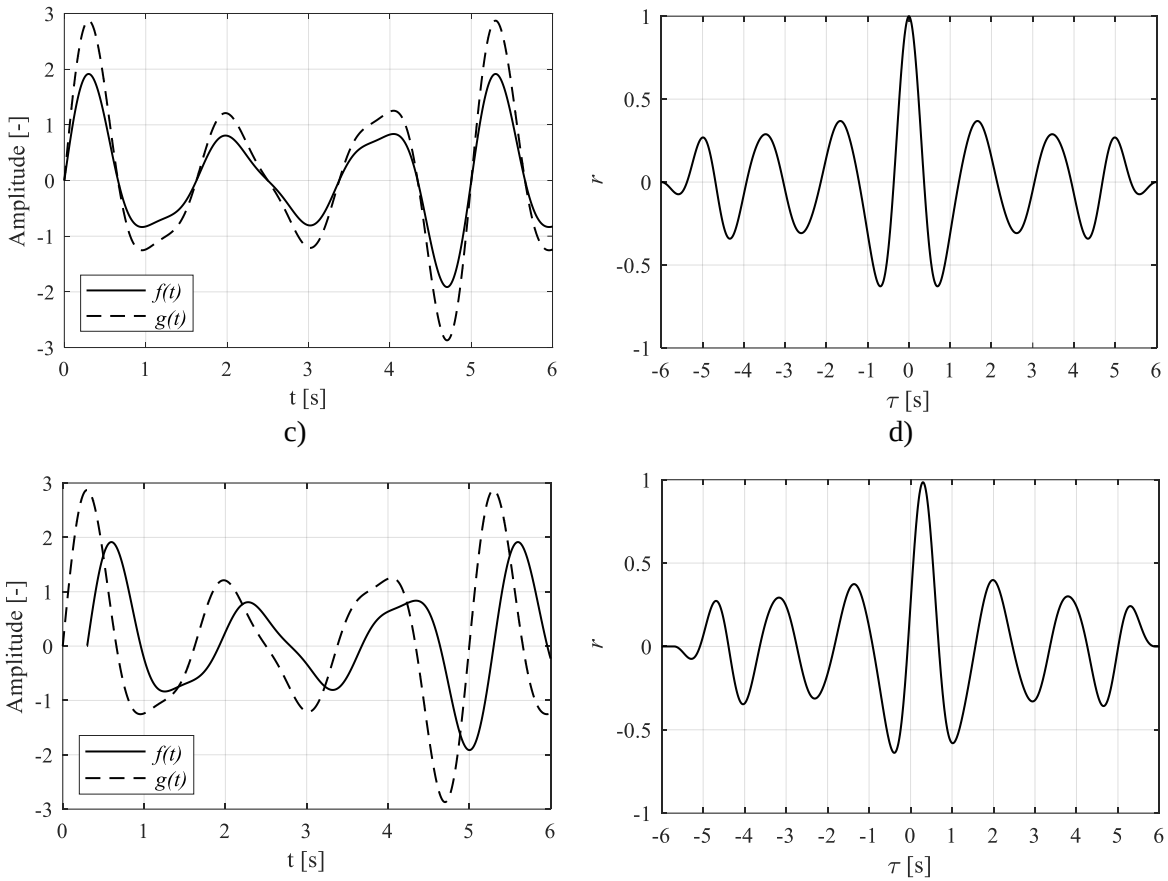

Figure 11: Example for the interpretation of the normalized cross correlation function *r*. Given arbitrary functions *f(t)* and *g(t)* in phase (a) and having a known time lag (c), together with the corresponding *r* functions (b-d, respectively).

Eq. (10) was applied to the experimental data by following the criteria discussed above. In Fig. 12, the evaluated normalized cross correlation between the local heat fluxes for the fixed axial coordinate z = 0.035 m over time, referred to channel 1 and 2, respectively (reference of Fig. 2), is shown for the same test cases of Fig. 10(a-b) and Fig. 10(c-d). In the horizontal orientation (Fig. 12a), the normalized cross correlation function assumes a peak ($r \approx 0.43$) for $\tau = 0$ s, denoting that the two considered heat fluxes independently oscillate with no time lag, i.e. the fluid is oscillating in parallel in both channels between the evaporator and the condenser. On the contrary, in the BHM (Fig. 12b), $r(\tau)$ assumes a peak ($r \approx 0.76$) for $\tau = 1.6$ s, denoting that both the positive and negative heat flux peaks exhibit a perceivable delay from one channel to the other. Here, the wall-to-fluid thermofluidic interactions result in either in-series warm-ups or cool-downs of the PHP channels, suggesting that the fluid is circulating along the entire device. Moreover, the positive sign of the time delay highlights that the fluid crosses channel 2 in advance, in accordance whit the fluid flow direction assessed by means of graph of Fig. 10d.

a)

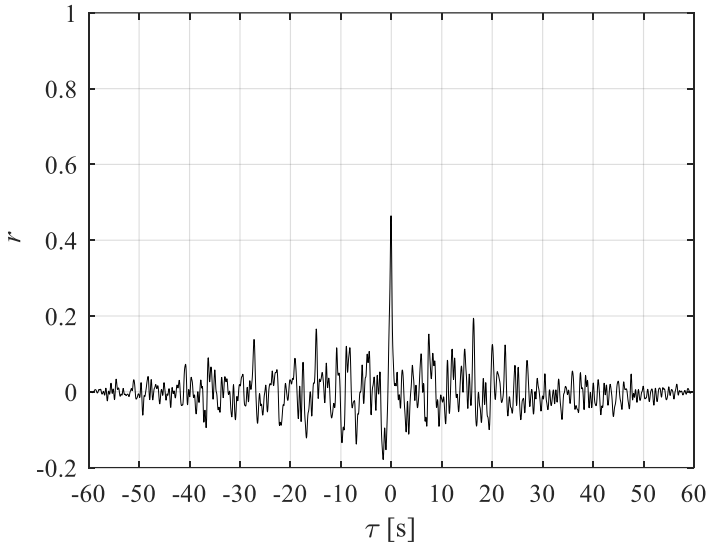

b)

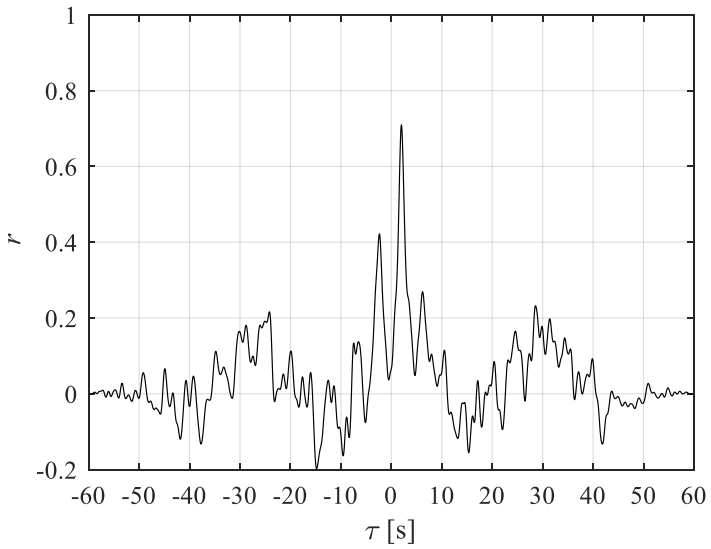

Figure 12: Normalized cross correlation function, evaluated by using the local wall-to-fluid heat fluxes referred to channel 1 and 2 for the fixed axial coordinate z = 0.035 m over time. Horizontal orientation, Q = 120 W, T_{cond} = 20°C (a); BHM, Q = 120 W, T_{cond} = 20°C (b).

4.5 Comprehensive heat transfer behaviour

To provide a comprehensive description of the PHP heat transfer behaviour under the studied working conditions, the statistical coefficients (cvt_{av} and cvt_{std}) and the flow motion type, evaluated in Sections 4.3 and 4.4, respectively, are listed in Table 4, together with the working modes presented in Table 3.

As already highlighted in Section 4.1, the device performance is independent of gravity within the high power input zone ($Q \geq 120$ W). For high heat loads, the device is fully activated for almost every considered configuration, thus suggesting that a regular fluid motion in the overall system promotes the independency of the PHP from orientation. Moreover, since the full activation is characterized by both fluid oscillations and circulations depending on the working conditions, as shown in Section 4.4, no significant relation between the flow motion type and the PHP performance can be assessed. Although the circulatory flow is preferable in planar geometries to achieve higher heat transfer performances, the

present 3D layout seems not to be greatly influenced by the circulatory flow at high power input levels, in accordance with the data provided in [31] for a similar 3D CLPHP geometry. However, the local thermofluidic interactions between the working fluid and the PHP wall may exhibit great variations from the oscillatory to the circulatory flow motion. To investigate such dependency, the 80th percentile of the local wall-to-fluid heat flux distributions [14] is shown in Fig. 13 as a function of Q for the horizontal and BHM configurations. Here, q_{80} significantly increases with Q in the horizontal configurations up to 6000 W/m^2, denoting strong local thermal interactions during the oscillatory flow at high heat loads to the evaporator. On the contrary, the exchanged wall-to-fluid heat fluxes within the adiabatic section for the BHM configurations settle to an almost constant low value for Q > 90 W, probably due to the fact that, when the circulatory flow occurs, the PHP tends to approach the thermal equilibrium in the adiabatic section. This results in weaker local wall-to-fluid thermal interactions, more comparable with the only heat dissipations to the surrounding environment by both natural convection and radiation at the adiabatic section, which are assumed to be, for the present application, lower than 300 W/m^2. This value is furthermore comparable with the q_{80} referred to low power inputs to the evaporator, where the device is not yet activated, and the heat exchanged between the PHP walls and the working fluid is almost equal to that exchanged with the environment.

As already mentioned, despite the higher amplitudes of the local wall-to-fluid heat flux, the thermal performance of the device (Fig. 5a) at high heat loads does not present any significant variations. This suggests that the heat stored or released by the channels wall within the adiabatic section, i.e. the evaluated local wall-to-fluid heat flux, is just a result of stronger interactions between the evaporator and the condenser section in terms of fluid motion, and it only presents a weak link with the total heat dissipated by the condenser. For the evaluation of the 80th percentile of the local wall-to-fluid heat flux q_{80}, the adopted samples were greater than 2 million (N·M·number of aluminium turns) for each heat load, thus providing a significant description of the local wall-to-fluid thermal interactions from a statistical standpoint.

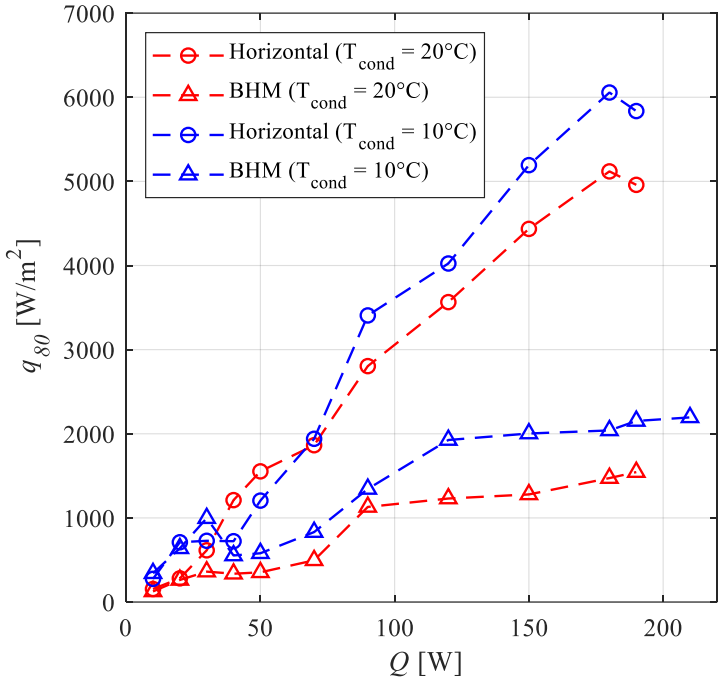

Figure 13: q_{80} as a function of the power input given to the evaporator, for every PHP configuration.

To deeper investigate the link between the global and the local heat transfer behaviour of the device, the thermal resistance was finally compared with the statistical coefficients cvt_{av} and cvt_{std}, previously adopted in Section 4.3 for a quantitatively description of the working modes.

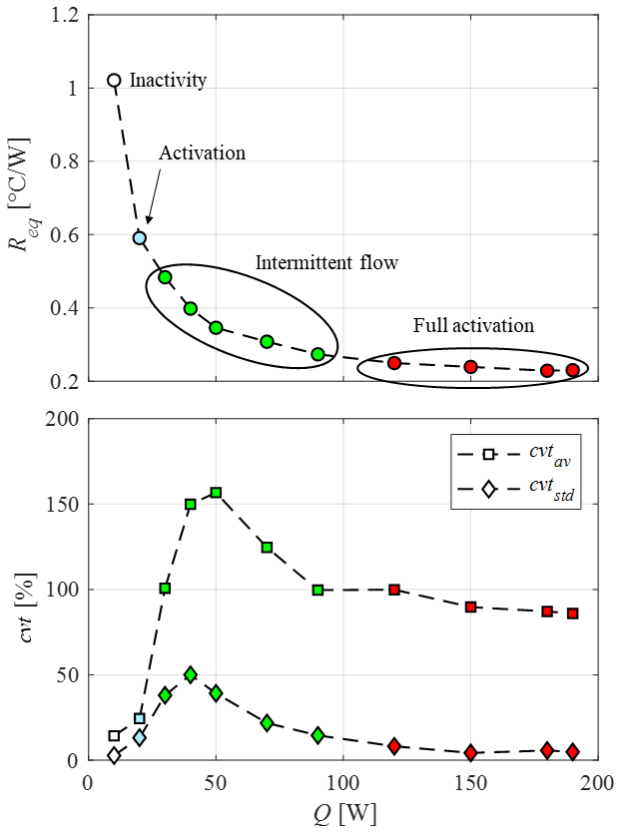

Figure 14: Comparison between the device thermal resistance and the statistical coefficients cvt_{av} and cvt_{std}, for the horizontal orientation, T_{cond} = 20°C.

Table 4: Working modes, flow motion types and statistical coefficients cvt_{av} and cvt_{std}, for every analysed configuration. "O": fluid oscillation, "C": fluid

		Q [W]											
		10	*20*	*30*	*40*	*50*	*70*	*90*	*120*	*150*	*180*	*190*	*210*
Orientation		***T_{cond} = 20°C***											
Horizontal	*Working mode*	-	*S*	*I*	*I*	*I*	*I*	*I*	*FA*	*FA*	*FA*	*FA*	
	Flow type	-	*O*	*O*	*O*	*O*	*O*	*O*	*O*	*O*	*O*	*O*	
	cvt_{av} [%]	*14.3*	*24.4*	*100.7*	*149.9*	*156.7*	*124.6*	*99.6*	*99.9*	*89.7*	*87.1*	*85.9*	
	cvt_{std} [%]	*2.8*	*13.2*	*38.1*	*50.1*	*39.2*	*21.8*	*14.6*	*8.2*	*4.3*	*5.7*	*4.9*	
BHM	*Working mode*	-	-	*S*	*I*	*I*	*I*	*FA*	*FA*	*FA*	*FA*	*FA*	
	Flow type	-	-	*O*	*O*	*O*	*O*	*C*	*C*	*C*	*C*	*C*	
	cvt_{av} [%]	*18.1*	*15.4*	*31.4*	*50.9*	*49.3*	*88.9*	*77.1*	*74.8*	*73.7*	*72.3*	*71.1*	
	cvt_{std} [%]	*4.8*	*4.8*	*17.7*	*23.9*	*26.9*	*48.4*	*2.8*	*4.3*	*2.8*	*2.4*	*2.3*	
THM	*Working mode*	-	-	-	-	*S*	*I*	*I*	*FA*	*FA*	*FA*		
	Flow type	-	-	-	-	*O*	*O*	*O*	*O*	*O*	*O*		
	cvt_{av} [%]	*20.5*	*15.4*	*16.2*	*16.2*	*17.4*	*21.4*	*33.3*	*82.2*	*94.5*	*84.7*		
	cvt_{std} [%]	*4.9*	*1.7*	*1.6*	*3.1*	*4.7*	*1.9*	*3.3*	*14.8*	*4.8*	*4.5*		
		T_{cond} = 10°C											
Horizontal	*Working mode*	-	*S*	*I*	*I*	*I*	*I*	*I*	*I*	*FA*	*FA*	*FA*	
	Flow type	-	*O*	*O*	*O*	*O*	*O*	*O*	*O*	*O*	*O*	*O*	
	cvt_{av} [%]	*11.3*	*73.7*	*31.0*	*47.9*	*80.4*	*115.8*	*130.8*	*91.8*	*101.3*	*93.8*	*97.8*	
	cvt_{std} [%]	*4.0*	*19.1*	*9.9*	*41.9*	*41.3*	*29.6*	*20.3*	*21.6*	*12.0*	*7.2*	*8.5*	
BHM	*Working mode*	-	-	-	-	-	*S*	*I*	*FA*	*FA*	*FA*	*FA*	*FA*
	Flow type	-	-	-	-	-	*O*	*O*	*C*	*C*	*C*	*C*	*C*
	cvt_{av} [%]	*15.3*	*14.3*	*15.8*	*16.5*	*22.0*	*35.7*	*86.0*	*75.8*	*77.3*	*75.9*	*72.2*	*72.9*
	cvt_{std} [%]	*10.5*	*4.5*	*3.7*	*5.0*	*19.9*	*26.1*	*8.9*	*6.0*	*4.5*	*3.8*	*2.7*	*2.6*
THM	*Working mode*	-	-	-	-	-	-	*S*	*I*	*I*			
	Flow type	-	-	-	-	-	-	*O*	*O*	*O*			
	cvt_{av} [%]	*15.3*	*14.3*	*14.6*	*12.1*	*11.0*	*27.0*	*148*	*157.3*	*121.3*			
	cvt_{std} [%]	*3.6*	*3.7*	*2.6*	*1.8*	*1.6*	*13.4*	*34.7*	*29.0*	*15.5*			

In Fig. 14, such comparison is referred to the horizontal orientation, T_{cond} = 20°C. When the device is inactive (white markers), the thermal resistance assumes a high value since the heat is only transferred by conduction. The device activation (light blue markers), denoted by a sudden increase in both cvt_{av} and cvt_{std} which exceed the activation threshold quantified in Section 4.3, is also characterized by an abrupt drop in the thermal resistance. Within the intermittent flow (light green markers), the thermal resistance keeps decreasing with a descending slope, and progressively approaches an asymptotic value. When the device is fully activated (dark green markers), the stable oscillatory flow in the whole device guarantees a low and almost constant thermal resistance. In Fig. 15, the same comparison is carried out on the BHM, T_{cond} = 20°C. Here, cvt_{av} and cvt_{std} present a sharp increase at Q = 30 W, i.e. such power input to the evaporator promotes the device activation, as also qualitatively observed in Fig. 7b. During the intermittent flow mode, the BHM presents a lower overshoot of both cvt_{av} and cvt_{std} with respect to the horizontal orientation, suggesting that the gravity forces stabilize the local thermal interactions between the PHP wall and the working fluid. Additionally, during the transition between intermittent flow and full activation, cvt_{std} exhibit a discontinuity in the BHM, denoting that the device thermal behaviour undergoes a sharp change in terms of regularity of the wall-to-fluid thermofluidic interactions in the overall device due to the establishment of the circulatory flow.

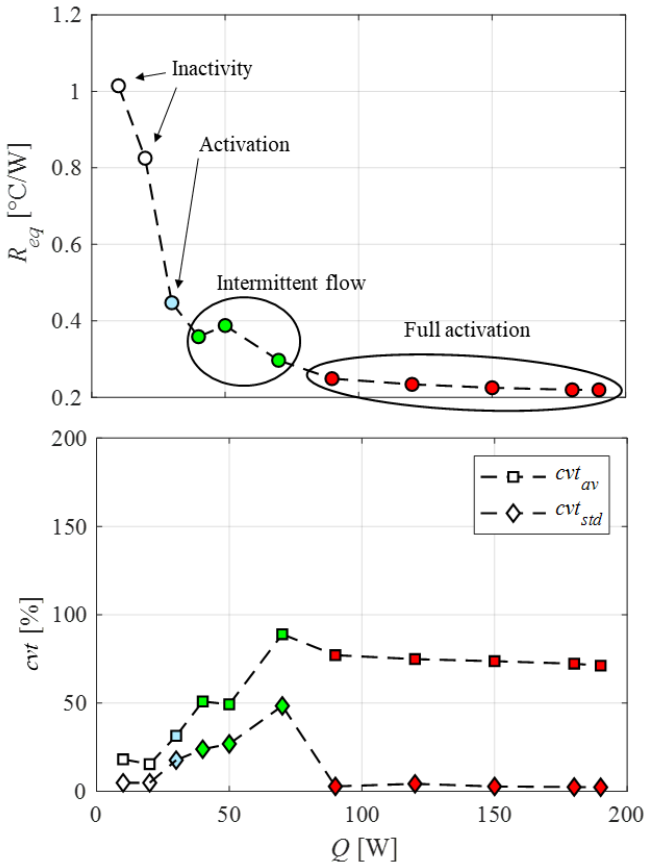

Figure 15: Comparison between the device thermal resistance and the statistical coefficients cvt_{av} and cvt_{std}, for the BHM, T_{cond} = 20°C.

5. Conclusions

A 14-turns three-dimensional Closed Loop Pulsating Heat Pipe made of annealed aluminium and partially filled with methanol was studied with the aim of assessing the effects of gravity and viscosity on its global and local thermal behaviour at varying heat loads. The device was first characterized by adopting the evaporator and condenser temperature, measured during the pseudo-steady state by means of thermocouples. The local wall-to-fluid heat flux exchanged within the adiabatic section was therefore

evaluated through an inverse approach, starting from thermographic acquisitions. A statistical approach on the resulting local heat transfer data was employed to quantitatively describe the working modes occurring during the Pulsating Heat Pipe operation by means of two coefficients of variation, namely cvt_{av} and cvt_{std}. The local wall-to-fluid heat flux was also adopted, together with the working fluid pressure and the evaporator temperature, to discern fluid oscillations from net fluid circulations. A comprehensive summarization of the statistical quantities, the working modes, the flow motion types and the evaluated equivalent thermal resistances was finally presented to deeper investigate the link between local and global quantities on the device response in different working configurations. The main outcomes of the present experimental work are listed below:

- The Pulsating Heat Pipe equivalent thermal resistance at low power inputs to the evaporator is strongly dependent on the chosen device configuration. For high power inputs, the studied three-dimensional layout exhibits instead comparable global performances in almost every considered configuration, with equivalent thermal resistances around 0.25 K/W, thus denoting an independent working behaviour of gravity.
- During the transition from inactivity to full activation, cvt_{av} reaches a maximum peak around 155% for the horizontal mode (T_{cond} = 20°C) and the Top Heated Mode (T_{cond} = 10°C), while it settles in the range 70 to 100% within the full activation for every Pulsating Heat Pipe configuration. Similarly, cvt_{std} denotes a maximum peak around 50% for the horizontal mode (T_{cond} = 20°C) and the Bottom Heated Mode (T_{cond} = 20°C) within the intermittent flow, while it approaches an asymptotic trend in the range 3 to 9% within the device full activation.
- The fluid net circulation occurred only during the Bottom Heated Mode in the ranges 90 to 190 W and 120 to 210 W for T_{cond} = 20°C and T_{cond} = 10°C, respectively. No significant relation between the circulatory motion and the global performance could be assessed, while the local heat transfer behaviour presents great differences from the oscillatory to the circulatory motion.
- The device performance is independent of the orientation during full activations, i.e. when a regular fluid motion is perceivable in every branch within the adiabatic section.

In conclusion, the considered three-dimensional geometry presents enhanced thermal performances with respect to the planar layouts even in unfavourable orientations. Such interesting feature is noticeable especially at high power inputs, where the device thermal performance in the Bottom Heated Mode, i.e. the generally best orientation for planar geometries, is comparable to that assessed for both the horizontal orientation and the Top Heated Mode which is generally the most unfavourable condition for planar geometries. The here employed statistical approach based on the device local heat transfer behaviour greatly improves the comprehension of the Pulsating Heat Pipes thermal response in pseudo-steady state conditions with respect to the only global performance. In future works, such approach will be extended to other geometries or working conditions.

The adopted in-depth analysis of the device operation through an extensive experimental campaign in ground conditions represents the natural evolution and completion of a previous characterization in microgravity. The provided results are thus of great relevance for the implementation of future tests on the International Space Station, scheduled in 2024.

Acknowledgments

The work has been carried out through a fruitful and effective collaboration between the University of Parma and the University of Pisa. The Authors would like to acknowledge the European Space Agency (ESA) support through the grant 4000128640/19/NL/PG/pt, ESA MAP project TOPDESS.

Nomenclature

Symbol	Quantity	SI Unit
c_p	Specific heat at constant pressure	J/kg·K
cvt	Coefficient of variation (time)	%
cvt_{av}	Mean of the coefficient of variations over the whole device	%

cvt_{std}	Standard deviation of the coefficients of variation over the whole device	%
H	Transfer function	-
k	Thermal conductivity	W/m·K
M	Number of time samples of the generic thermographic temperature distribution	-
N	Number of axial coordinates of the generic thermographic temperature	-
q	Convective heat flux per unit surface	W/m^2
Q	Power input provided to the evaporator	W
r	Normalized cross-correlation function	-
R_{env}	Overall heat-transfer resistance between the external tube wall and the surrounding environment	$m^2 \cdot K/W$
R_{eq}	Equivalent thermal resistance	K/W
t	Time	s
T	Temperature	K, °C
u, v	Frequency components	rad^{-1}
u_c	Cut-off frequency	rad^{-1}
z	Axial coordinate	m
ΔP	Fluid pressure difference between the evaporator and the condenser section	Pa
ρ	Density	kg/m^3
σ	Noise level	K, °C
τ	Time lag	s

Subscripts, superscripts

80	80^{th} percentile
cond	condenser
env	environment
eva	evaporator
f	filtered
n	n-th channel

References

[1] S. M. Sohel Murshed and C. A. Nieto de Castro, "A critical review of traditional and emerging techniques and fluids for electronics cooling", Renew. Sustain. Energy Rev., 78 (2017), 821–833.

[2] V. Nikolayev, M. Marengo, Pulsating heat pipes: basics of functioning and numerical modeling, ISBN 978-981-3234-36-9, in: J.R. Thome (Ed.), Encyclopedia of Two-Phase Heat Transfer and Flow IV, vol. 1 Modeling of Two-Phase Flows and Heat Transfer, World Scientific, 2018.

[3] D. Bastakoti, H. Zhanga, D. Lia, W. Caia, F. Li, An overview on the developing trend of pulsating heat pipe and its performance, App. Therm. Eng. 141 (2018) 305–332.

[4] X. Han, X. Wang, H. Zheng, X. Xu, G. Chen, Review of the development of pulsating heat

pipe for heat dissipation, Renewable and Sustainable Energy Reviews, 59 (2016) 692–709.
[5] M. Mameli, L. Araneo, S. Filippeschi, L. Marelli, R. Testa, M. Marengo, Thermal response of a closed loop pulsating heat pipe under a varying gravity force, International Journal of Heat and Mass Transfer, 80 (2014), 11-22.
[6] Y. Zhang, A. Faghri, Advances and unsolved issues in pulsating heat pipes, Heat Transfer Engineering, 29 (2008), 20–44.
[7] P. Charoensawan, S. Khandekar, M. Groll, P. Terdtoon, Closed loop pulsating heat pipes Part A: parametric experimental investigations, International Journal of Heat and Mass Transfer, 16, (2003), 2009-2020.
[8] J. Lee, Y. Joo, S. J. Kim,Effects of the number of turns and the inclination angle on the operating limit of micro pulsating heat pipes 124 (2018), 1172-1181.
[9] H. Yang, S. Khandekar, M. Groll, Operational limit of closed loop pulsating heat pipes, Applied Thermal Engineering, 28 (2008), 49-59.
[10] J. Qu, J. Zhao, Z. Rao, Experimental investigation on the thermal performance of three-dimensional oscillating heat pipe, International Journal of Heat and Mass Transfer, 109 (2017), 589-600.
[11] J. Qu, J. Zhao, Z. Rao, Experimental investigation on thermal performance of multi-layers three-dimensional oscillating heat pipes, International Journal of Heat and Mass Transfer, 115 (2017), 810-819.
[12] C. Y. Tseng, K. S. Yang, C. C. Wang, Non-Uniform Three-Dimensional Pulsating Heat Pipe for Anti-Gravity High-Flux Applications, Energies, 13(12):3068, 2020.
[13] M. Mameli, A. Catarsi, D. Mangini, L. Pietrasanta, N. Michè, M. Marengo, P. Di Marco, S. Filippeschi, Start-up in microgravity and local thermodynamic states of a hybrid loop thermosyphon/pulsating heat pipe, Applied Thermal Engineering, 158 (2019), 113771.
[14] L. Pagliarini, L. Cattani, F. Bozzoli, M. Mameli, S. Filippeschi, S. Rainieri, M. Marengo, Thermal characterization of a multi-turn pulsating heat pipe in microgravity conditions: Statistical approach to the local wall-to-fluid heat flux, International Journal of Heat and Mass Transfer, 169 (2021), 120930.
[15] R. R. Riehl, S. M. S. Murshed, Life Time Expectancy Prediction and Ageing Process of Heat Pipes Using Nanofluids, Heat Transfer Engineering, 2020.
[16] C. D. Henry, J. Kim, B. Chamberlain, Heater size and heater aspect ratio effects on sub-cooled pool boiling heat transfer in low-g, in: 3rd International Symposium on Two-phase Flow Modeling and Experimentation Pisa, 22-24 September 2004.
[17] Beck J.V., Balckwell B., St. Clair Jr C.R., Inverse Heat Conduction – Ill-posed problems, New York: John Wiley & Sons Inc. 1985.
[18] Murio A.D., The Mollification Method and the Numerical Solution of Ill-Posed Problems, New York: John Wiley and Sons 1993.
[19] Delpueyo D., Balandraud X., Grédiac M., Heat source reconstruction from noisy temperature fields using an optimised derivative Gaussian filter, Infrared Physics & Technology *60* (2013) 312–322.
[20] Bozzoli F., Pagliarini G., Rainieri S., Experimental validation of the filtering technique approach applied to the restoration of the heat source field, Experimental Thermal and Fluid Science, 44 (2013) 858-867.
[21] Morozov V.A., Methods for Solving Incorrectly Posed Problems, Springer-Verlag, New York, (1984).
[22] S. Kline and F. McClintock, “Describing Uncertainties in Single-Sample Experiments,” Mechanical Engineering, 75 (1953), 3-8.
[23] B. Verma, V. J. Yadav, K. Kumar, Experimental Studies on Thermal Performance of a Pulsating Heat Pipe with Methanol/DI Water, Journal of Electronics Cooling and Thermal Control, 3(2013).
[24] M. Mameli, V. Manno, S. Filippeschi, M. Marengo, Thermal instability of a Closed Loop Pulsating Heat Pipe: Combined effect of orientation and filling ratio, Experimental Thermal and Fluid Science, 59(2014), pp 222-229.

[25] V. Ayel, L. Areneo, A. Scalambra, M. Mameli, C. Romestant, A. Piteau, M. Marengo, S. Filippeschi, Y. Bertin, Experimental study of a closed loop flat plate pulsating heat pipe under a varying gravity force, International Journal of Thermal Sciences, 96(2015), pp 23-34.
[26] Cattani, L., Mangini, D., Bozzoli, F., Pietrasanta, L., Mameli, M., Filippeschi, S., ... & Marengo, M. (2019). An original look into pulsating heat pipes: Inverse heat conduction approach for assessing the thermal behaviour. Thermal Science and Engineering Progress, 10, 317-326.
[27] G. Spinato, N. Borhani, J. R. Thome, Understanding the self-sustained oscillating two-phase flow motion in a closed loop pulsating heat pipe, Energy, 90 (2015), 889-899.
[28] X. Cui, Y. Z. Zhihua, L. S. Shun, Combination study of operation characteristics and heat transfer mechanism for pulsating heat pipe, Applied Thermal Engineering, 65 (2014), pp.394-402.
[29] K. Ishii, K. Fumoto, Temperature Visualization and Investigation Inside Evaporator of Pulsating Heat Pipe Using Temperature-sensitive Paint, Applied Thermal Engineering, 155 (2019), 575-583.
[30] P. Stoica and R. Moses, Spectra Analysis of Signals, Upper Saddle River, NJ: Prentice Hall, 2005.
[31] C. Feng, Z. Wan, H. Mo, H. Teng, Heat transfer characteristics of a novel closed-loop pulsating heat pipe with a check valve, Applied Thermal Engineering, 141 (2018), 558-564.